Published in final edited form as:

Biofabrication. ; 14(4): . doi:10.1088/1758-5090/ac8768.

Human gelatin-based composite hydrogels for osteochondral tissue engineering and their adaptation into bioinks for extrusion, inkjet, and digital light processing bioprinting

Matthew L. Bedell[1], **Angelica L. Torres**[1], **Katie J. Hogan**[1,2], **Ziwen Wang**[1], **Bonnie Wang**[1], **Anthony J. Melchiorri**[3], **K. Jane Grande-Allen**[1], **Antonios G. Mikos**[1,3]

[1]Department of Bioengineering, Rice University, Houston, TX

[2]Medical Scientist Training Program, Baylor College of Medicine, Houston, TX

[3]NIBIB/NIH Center for Engineering Complex Tissues, USA

Abstract

The investigation of novel hydrogel systems allows for the study of relationships between biomaterials, cells, and other factors within osteochondral tissue engineering. Three-dimensional (3D) printing is a popular research method that can allow for further interrogation of these questions *via* the fabrication of 3D hydrogel environments that mimic tissue-specific, complex architectures. However, the adaptation of promising hydrogel biomaterial systems into 3D-printable bioinks remains a challenge. Here, we delineated an approach to that process. First, we characterized a novel methacryloylated gelatin composite hydrogel system and assessed how calcium phosphate and glycosaminoglycan additives upregulated bone- and cartilage-like matrix deposition and certain genetic markers of differentiation within human mesenchymal stem cells (hMSCs), such as RUNX2 and SOX9. Then, new assays were developed and utilized to study the effects of xanthan gum and nanofibrillated cellulose, which allowed for cohesive fiber deposition, reliable droplet formation, and non-fracturing digital light processing-printed (DLP) constructs within extrusion, inkjet, and digital light processing techniques, respectively. Finally, these bioinks were used to 3D print constructs containing viable encapsulated hMSCs over a seven-day period, where DLP printed constructs facilitated the highest observed increase in cell number over seven days (~2.4×). The results presented here describe the promotion of osteochondral phenotypes *via* these novel composite hydrogel formulations, establish their ability to bioprint viable, cell-encapsulating constructs using three different 3D printing methods on multiple bioprinters, and document how a library of modular bioink additives affected those physicochemical properties important to printability.

Corresponding Author: Antonios G. Mikos; mikos@rice.edu, Rice University, P.O. Box 1892, MS-142, Houston, TX 77251-1892, Tel: (713) 348-5355 ; Fax: (713) 348-4244.

[7]·Author Contributions

Matthew L. Bedell: Conceptualization, methodology, software, investigation, supervision, project administration, data analysis and interpretation, writing original draft, writing revisions, writing final draft. **Angelica L. Torres**: Methodology, software, investigation, data analysis and interpretation. **Katie J. Hogan**: Conceptualization, methodology, investigation, supervision, data analysis and interpretation, writing final draft. **Ziwen Wang**: Methodology, software, investigation, data analysis and interpretation. **Bonnie Wang**: Software, investigation, data analysis and interpretation. **Anthony J. Melchiorri**: Supervision, project administration, funding acquisition. **Jane Grande-Allen**: supervision, methodology, data analysis and interpretation. **Antonios G. Mikos**: Conceptualization, methodology, writing revisions, writing final draft, supervision, project administration, funding acquisition.

The authors declare no competing conflicts of interest.

Graphical Abstract

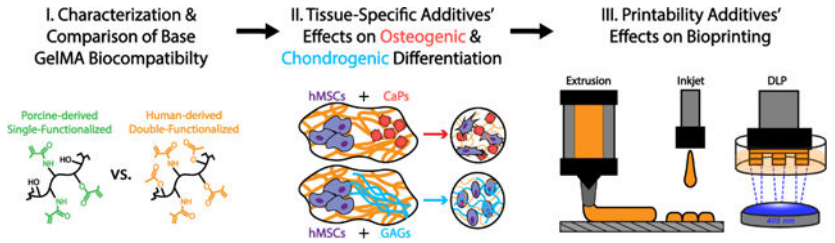

1. Introduction

Tissue engineering seeks to combine cells, growth factors, and scaffolds with external stimuli to regenerate or replace tissue [1]. The earliest kinds of scaffold fabrication included simple molding, sintering, electrospinning, and particulate leaching of metals, plastics, and hydrogels [2–5]. More recently, however, the use of hydrogels has dominated tissue engineering approaches, likely because of these materials' ability to encapsulate cells, match native tissue mechanical properties, and recapitulate the native aqueous extracellular environment and its diffusional characteristics [6]. Furthermore, the use of three-dimensional (3D) bioprinting in recent literature has catalyzed the initiation of studies seeking to investigate questions of scaffold complexity, as 3D printing's different modalities and accessible technology allow for construction of living tissue constructs with heterogeneous architectures, spatial patterns, and multiple cell types [1,7,8].

Osteochondral tissue is an example of this heterogeneous architecture. This junction joining articular cartilage to bone gradually transitions from the innermost region of subchondral bone to the outermost region of superficial cartilage, which functions as a friction-reducing and load-bearing cushion in synovial joints. The chondrocytes present here are essential to cartilage tissue function and originate from mesenchymal stem cells (MSCs) found in the bone marrow [9,10]. Chondrocytes replace degraded extracellular matrix (ECM) molecules to maintain adequate thickness and mechanical properties of the tissue in response to normal function and physiological loading [10,11].

Among those ECM molecules secreted are glycosaminoglycans (GAGs) such as hyaluronic acid (HyAc), dermatan sulfate, and heparan sulfate. Other proteins called proteoglycans associated with GAG chains to fill up most of the interfibrillar space of the ECM and contribute to much of the compressive stress distribution of cartilage through their ability to attract water [9,10]. HyAc is a non-sulfated GAG that is the most abundant and most ubiquitous of all the GAGs in human tissues and it possesses an inherent bioactivity and promotes cell proliferation and chondrogenic differentiation [12,13].

The transition from the GAG-laden, relatively soft tissue zone to the denser bone layers occurs through the calcified zone and subchondral bone layer, where hydroxyapatite, a calcium phosphate (CaP), can be found [9,14]. CaPs have been utilized in the form of micro- or nano-powders to create uniform or composite osteoconductive and osteoinductive scaffolds [15–18]. CaPs impart high mechanical strength and tunable degradation, from

resorption within a few months in the case of beta-tricalcium phosphate (β-TCP) to non-resorbable crystalline forms of hydroxyapatite [14,19,20].

To construct and study tissue-like architectures, such as the osteochondral junction discussed above, a variety of biomaterials have been used. As a base 3D printed bioink polymer, collagen is widely utilized since it is the most abundant fibrous protein found in mammalian tissues. Gelatin is denatured collagen that has lost its supramolecular fibril structure after being subjected to high temperatures, and it possesses many of the same biocompatibility and cell adhesive properties as collagen without needing similar sensitive titration methods for gelation [1]. Gelatin methacryloyl (gelMA) is the most common form of gelatin used in bioinks, along with radical initiators and other crosslinking molecules that might participate in covalent network formation for long-term cell culture studies [21,22]. GelMA is prepared most commonly via a two-phase reaction involving addition of methacrylic anhydride, though adjusting the many different aspects of the synthesis procedure including molar excess of reactants, the use of acetic anhydride, and stirring speed may affect the final degree of modification and consequent functional properties of the polymer within a particular bioink [22–24]. For adaptation of these materials into printable bioinks, common additives that dramatically modify viscosity at low concentrations, such as xanthan gum (XG) and nanofibrillated cellulose (NFC), have been found suitable for synthesizing printable inks and maintaining high cell viability within *in vitro* studies [25–32].

Within tissue engineering, various 3D printing tools have become increasingly available to researchers for the purpose of fabricating cell-laden constructs or tissue-like scaffolds. The most common bioprinting methods can be divided into extrusion, inkjet, and digital light processing (DLP) [1,33]. The choice of modality depends on the study, as the respective technology-specific limitations differ and may preclude approaches to printing a scaffold that mimics the properties of a given tissue [1,33–35]. The use of gelatin-based bioinks with CaPs or GAGs for osteochondral tissue engineering, with and without stabilizers like XG and NFC, has been employed within many recent works [1,27,36–44]. Still, the approach shown here of taking a single osteochondral hydrogel system and studying its printability over a spectrum of printing modalities, as well as the assays and experiments employed to achieve successful fabrication of constructs within each method, has not been documented within a single body of work. What is less common, too, is a thoroughly-vetted library of both crosslinkable base polymers, such as the gelMAs investigated here, as well as modular additives that have been studied for their suitability to compose a bioink that is able to fabricate tissue-specific 3D constructs. Thus, the documentation of adapting a well-characterized hydrogel system into a ‘universal bioink’ capable of printing in each modality would pass along ways to apply other hydrogel platforms to diverse 3D tissue engineering approaches, and would be highly valuable to the scientific community [45].

In the following studies, we sought to characterize a novel hydrogel system for osteochondral tissue engineering *via* three bioprinting modalities. Specifically, we investigated the ability for β-TCP and methacrylated hyaluronic acid (HAMA) to support growth and differentiation of gelMA-encapsulated human MSCs (hMSCs). We examined the effects of two candidate gelMA backbone polymers, β-TCP, and HAMA combinations and concentrations on viability, proliferation, extracellular matrix deposition, and upregulation of

lineage-specific mRNA markers in varied cell culture medium environments. Additionally, the effects of XG and NFC on each bioink's shear-dependent dynamic viscosity and retention of fiber or droplet shape were examined *via* oscillatory and flow rheology or printing experiments, respectively. This work also describes novel, high-throughput assays developed to understand the relationship between 3D printing parameters such as nozzle speed, cartridge pressure, inkjet valve timing, DLP projector crosslinking dosage, and UV dye concentration on the resulting resolution and printability of bioprinted constructs within each respective printing modality.

We hypothesized that less functionalized gelMA polymer will promote higher cell viability and proliferation by possessing fewer non-biodegradable network crosslinks, and that the inclusion of β-TCP or HAMA in gelMA compared to gelMA controls would increase each bioink's respective tissue-specific ECM deposition and upregulation of mRNA markers by hMSCs for differentiation in both tissue-specific culture medium and mixed media environments. Higher additive levels would also decrease hMSC proliferation due to those additives lacking the same integrin binding sites as they displace the cell-adhesive gelMA base hydrogel with their increasing weight percent. Additionally, we hypothesized that XG and NFC would increase low-shear dynamic viscosity and shear-thinning behavior in a dose-dependent manner, and that increasing these properties would both correspond with stable fiber and droplet formation and yield better qualitative 3D printing outcomes as assessed by standardized printability trials. Finally, when fabricating tissue engineering constructs that encapsulate hMSCs via extrusion, inkjet, or DLP bioprinting, we hypothesized that all bioprinting methods will yield constructs with similar encapsulated viability due to tradeoffs unique to each bioprinting method, such as how higher cytotoxic shear forces are present within nozzle-based inkjet and extrusion printing and how a dose-dependent cytotoxic UV absorber compound is utilized within DLP bioink formulations.

2. Materials and Methods

2.1 Materials

Porcine-derived gelatin mathacryloyl or single-functionalized gelatin (SF-gelMA), methacrylated hyaluronic acid (HAMA, derived from *Streptococcus zooepidemicus*), and lithium phenyl-(2,4,6-trimethylbenzoyl)phosphinate (LAP) were purchased from Allevi, Inc. (Philadelphia, PA). Human-derived gelatin methacryloyl or double-functionalized gelatin (DF-gelMA) was purchased from Humabiologics, Inc. (Phoenix, AZ). Non-modified porcine-derived gelatin was obtained from Nitta (Morrisville, NC). Maxgard 1800 (benzophenone-9, R1800) was obtained from Lycus (Lycus Ltd., El Dorado, AR). Glass-bottomed (#1.5H) 96-well plates were purchased from CellVis (Mountain View, CA). Bovine serum albumin (BSA), dexamethasone, ascorbic acid, sodium bicarbonate, Dulbecco's phosphate buffered saline (PBS), transforming growth factor β−3 (TGF-β3), Eagle's minimum essential medium alpha modification (α-MEM), xanthan gum, unsintered β-tricalcium phosphate (β-TCP, #13204), proteinase K, iodoacetamide, pepstatin A, von Kossa stain kit, acetic acid, hydrofluoric acid, Alcian Blue stain, Nuclear Fast Red stain, dimethylmethylene blue reagent (DMMB), and CS-2 CellStack high-volume culture chambers were all obtained from Sigma (MilliporeSigma, Burlington, MA). ITS+ Premix

Universal Cell Culture Supplement was purchased from Corning, Inc. (Corning, NY). Optimal cutting temperature compound, tris-ethylenediaminetetraacetic acid (Tris-EDTA), PicoGreen kits, LIVE/DEAD staining kits, TrypLE, and antibiotic-antimycotic were purchased from ThermoFisher Scientific (Waltham, MA). Stainless steel beads, RNEasy Mini Plus kits, lysis buffers, Qiashredder tissue lyser columns, and RNAprotect tissue reagent were purchased from Qiagen (Germantown, MD). iScript cDNA synthesis kit and iTaq universal SYBR green supermix were purchased from Bio-Rad Laboratories (Hercules, CA). Tapered-flow and needle luer lock extrusion tips were purchased from Nordstrom EFD (East Providence, RI). Fetal bovine serum (Benchmark™ FBS) was purchased from GeminiBio (West Sacramento, CA). Nanofibrillated cellulose (NFC) was purchased from Cellink (Boston, MA). Arsenazo III reagent was purchased from Pointe Scientific (Canton, MI). CellTiter-Glo 3D Cell Viability assay and the CellTox Green kit was purchased from Promega (Madison, WI). Alizarin Red S stain was purchased from Sciencell (Carlsbad, CA). Bone marrow derived mesenchymal stem cells (hMSCs) and their associated expansion medium were purchased from ATCC, Inc. (ATCC ® PCS-500–012, Manassas, VA) and RoosterBio (Lot #3210264, Sex: Female, Age: 20 yr, CD34 & CD45 antigen: <10% positive, CD90 & CD166 antigen: >90% positive, Frederick, MD).

2.2 Expansion of hMSCs

For the encapsulated metabolic activity experiment, bone marrow-derived hMSCs (bm-hMSCs) (ATCC, Manassas, VA) were seeded in T-225 flasks according to the manufacturer's recommendation. Cells were expanded in an hMSC growth medium formula consisting of α-MEM, 20% FBS, and 1% antibiotic-antimycotic. Cells were passaged at ~80–90% confluency and harvested for experiments by passage five. For all other cell culture experiments, bm-hMSCs were expanded using RoosterBio high-volume cell culture kits and cells. Cells were either cultured in T-225 flasks or CS-2 CellStack chambers according to the recommended seeding density and final desired cell count. The manufacturer's cell-specific media with growth factor supplementation was used, with media changed every 3 days. Cells were passaged and harvested at 80–90% confluency and by passage five for viability experiments or by passage number three for differentiation experiments. An incubator set to 95% humidity at 37 °C and 5% CO_2 was utilized for all cell culturing and expansion. PBS was used to wash away dead cells and TrypLE was used to detach cells. To form a pellet for resuspension, cells were centrifuged at 200*g for 5 min. To count cell populations, a standard visual hemocytometer was used.

2.3 Cell resuspension and bioink crosslinking for encapsulated viability and proliferation studies

Each bioinks' effects on cell viability and proliferation were studied based on a modification to a previously reported high-throughput method [46]. Briefly, upon reaching the target confluency and passage number, cells were counted, centrifuged, and resuspended thoroughly via pipette in 0.2 mL of cell culture media at 5× final cell density. To that microcentrifuge tube, 0.8 mL of 1.2× concentrated bioink was added such that the final concentration was 1× when including the cell suspension. After mixing via positive displacement pipette, 10 μL of bioink was deposited into a microscopy-suited, glass-bottom well plate (n=5). Each droplet was confirmed to not make contact with the well sides and

then crosslinked using excess energy with a 405 nm lightguide (Dymax, Torrington, CT) for 4 seconds at 1.3 W/cm^2, which is 4× the manufacturer recommendation for the gelMA materials, to compensate for any commercial batch variability and ensure most reactive sites had crosslinked. Afterwards, all samples were washed with PBS to lift any non-encapsulated cells, and then 150 μL of growth medium was added and exchanged every 3 days.

To assess viability and proliferation via metabolic activity, adenosine triphosphate ATP quantification was used at 2 and 24 hr with a CellTox Green cytotoxicity assay (n=5) [46]. Briefly, a vial of CellTiter-Glo 3D Viability assay was fully thawed and applied in 100 μL aliquots to all bioink samples after they had been washed for 30 min in PBS and cooled to room temperature. The plate was covered in foil, and then incubated for 30 min on an orbital shaker to induce lysis an encourage binding of ATP to the reporter. Using a Spectramax M2 plate reader (Molecular Devices, San Jose, CA), the luminescent signals were read at 15 reads per well. CellTox green was then applied according to the manufacturer's protocols and read for it's fluorescent signal, which binds to dead cells' DNA. All signals of experimental groups containing combinations of the β-TCP and HAMA additives were divided by the signal of an additive-free control group. The control groups were set as 100% relative viability/proliferation.

To assess encapsulated viability via assessment of cell death, a modification of a method detailing an extended Live/Dead stain was utilized [46]. Briefly, the calcein AM and ethidium homodimer-1 solutions were prepared according to the manufacturer's instructions. After soaking all bioink samples in warm PBS for at least 30 min to remove residual cell culture medium, 100 μL of the combined stain was applied for 30 min at 2 and 24 hr after experiment initiation. Due to the opacity of suspended β-TCP particles precluding *z*-stack scanning through the sample, a confocal fluorescent microscope was used to stitch a 9×9 fields of view into a composite image at 10× magnification at least 100 μm above the bottom layer of the glass into the cell-laden sample. Live cell signals were captured as green fluorescence in the 515 nm emission channel and dead cells were captured as red fluorescence within the 635 nm emission channel (Supp. Fig. 1). The composite field of view images were exported to Fiji (open-source software, https://imagej.net/software/fiji/), which processed the images such that the autofluorescence of the β-TCP particles were ignored and only the brightest signals, the cells, were counted (Supp Fig. 2). Viability was reported as the number of living cells divided by the total number of living and dead cells counted within each sample (n=5).

2.4 Pre-processing of acidic composite bioink components to buffer pH effects

To mitigate the drop in pH observed when mixing the untreated bioink precursors β-TCP and gelMA polymers into aqueous PBS solution, two approaches to buffering the pH were used, with all associated data shown in Supp. Fig. 3. First, β-TCP was suspended within PBS at 0.25% w/v and mixed for 24 hr at 100 RPM at 37 °C. Afterwards, the suspension was vacuum filtered, and the filter paper with the adhered ceramic particles was placed in a lyophilizer for 24 hr. The dried ceramic material, now aggregated into flakes, was then collected into a glass vial and dispersed via sonicating wand at 50% power for 2 min (Q125, QSonica, Newtown, CT) [47]. Following this step, the powder was filtered using a 100 μm

metal sieve to remove any remaining large aggregates. The buffered material was confirmed to maintain a cell-friendly pH of 7.2 ± 0.2 following measurement with a standard pH meter after resuspension in PBS. All gelMA bioinks were dissolved at 10% w/v in PBS and buffered with 1.25 mg/mL of $NaHCO_3$, which was the minimum mass empirically determined to achieve a pH of >7 for a 10% w/v gelMA solution.

2.5 Assessment of hMSC cytotoxicity using bioink leachable molecules

To investigate the cytotoxicity of leachable content, crosslinked hydrogels were soaked in medium and exposed to cell monolayers to measure the effect on viability [48]. All composite bioink hydrogel components were sterilized *via* 24 hr of ethylene oxide exposure or germicidal UV for at least 6 hr before gel fabrication. Gels were crosslinked with 405 nm at the same irradiance and intensity within 30 μL Teflon molds, and then incubated with serum free growth medium at 1 mL per cm^2 of gel surface area (n=4). After 24 hr of incubation with α-MEM, that leaching medium was sterile-filtered and stored. Separately, bm-hMSCs were expanded using hMSC growth medium and seeded into a black, opaque 96-well plate at 15,000 cells per well. After reaching ~90% confluency, the medium was aspirated, the cell monolayers were washed once in warm PBS, and then the PBS was replaced with 1×, 10×, and 100× dilutions of 100 μL of filtered leachables medium (n=5). Monolayers for the 'Live' and 'Dead' control were included, which were exposed to fresh serum-free medium. After 2 and 24 hr, the medium was aspirated and replaced with 100 μL of warm PBS for 5 min. For the Dead control, 100 μL of 70% ethanol was applied for 5 min. Then, all wells' media were replaced with 100 μL of prepared calcein AM/ethidium homodimer-1 staining solution.

After 30 min of incubation at room temperature in the dark, wells were measured for 515 nm ('Live') fluorescence and 617 nm ('Dead') fluorescence using a BioTek Instruments (Winooski, VT) FLx800 fluorescence plate reader. The signal from the Live control group was set as 100% relative viability, and the Dead signal of the Dead control group was set as 100% relative cytotoxicity. The respective Live or Dead signals of each experimental group were divided by the average fluorescence value of those control groups.

2.6 Comparison of gelMA polymers via photorheology, characterization of molecular weight, and assessment of degree of functionalization

Bioinks' changes in viscoelastic properties after crosslinking were investigated using broad spectrum ultraviolet light on a quartz glass-equipped rheometer (Discovery HR-2, New Castle, DE). After enabling automatic *z*-axis control to compensate for any gel shrinkage, non-crosslinked samples that had been warmed to 37 °C in a solution state were subject to an initial 30 s equilibration period and then crosslinked in oscillation mode with 1 Hz sampling within a 500 μm geometry gap under a 20 mm steel plate at 10 mW/cm^2 for 5 min. For comparisons of molecular weights, both gelMA polymers were subjected to aqueous gel permeation chromatography (GPC) (Waters ACQUITY Advanced Polymer Chromatography System, Waters, Milford, MA) and compared to a set of 10–80 kDa poly(ethylene glycol) standards. All materials were sterile filtered and dissolved in 0.1 M $NaNO_3$ at 10 mg/mL before column injection, and data was analyzed within Empower 3 software (Waters).Here, the Mark-Houwink equation was used within the Empower processing software (Waters,

Milford, MA) to obtain the universal calibration curve from PEG standards and the exact molecular weight of these gelMAs [49–51]. For PEG, constants of $K=10.1\times10^{-2}$ mL/g and a=0.58 were used [52]. The constants for both gelMAs were approximated from previously reported measurements of bovine gelatin, $K=8.4\times10^{-6}$ mL/g and a = 0.88 [53,54]. For determination of relative degrees of methacryl content, a sample of porcine-derived gelatin and both gelMA polymers were sterile filtered and dissolved in deuterium oxide with 0.05 wt% of trimethylsilylpropanoic acid (TMSP) as reference at a concentration of 25 mg/mL. Then, using ^{1}H Nuclear Magnetic Resonance (^{1}H NMR) spectroscopy at 40 °C, the absorbance peaks were analyzed at 600 MHz using Bruker equipment and software (Bruker BioSpin spectrometer, Billerica, MA). Peaks were quantified using methods put forward specifically for analyzing gelMA, where phenylalanine peaks (7.2–7.5 ppm) were used to normalize the integrals of total methacryl content (5.3–6.3 ppm), respectively [24].

2.7 Mass loss and pH study of crosslinked gels incubating in PBS

An enzyme-free 28-day mass loss study was initiated to understand the degree to which the CaP additive and non-crosslinked SF-gelMA or DF-gelMA were retained in the hydrogel systems. PBS incubating medium was exchanged every 3 days at 37 °C on a 100 RPM oscillating table. 90 μL of bioink was pipetted into a 3 mm tall by 6 mm diameter cylindrical Teflon mold and fully crosslinked with 405 nm light using the previously described dosage. Gels were then placed individually into a 12-well plate, combined with 3 mL of 2% w/v antibiotic-antimycotic-containing PBS, covered and sealed inside autoclave bags for added sterility, and then allowed to incubate (n=3). The chosen volume of PBS per gel was 2× higher than the other *in vitro* experiments to better maintain a diffusion gradient that leached any non-crosslinked material. The pH was measured optically and non-invasively before each PBS exchange using an SBI Developer's Kit (ScientificBio, Pittsburgh, PA). At each timepoint, gels were harvested, lyophilized, and measured for their dry mass, which was divided by the mass of samples measured immediately after gel fabrication.

2.8 *In vitro* study of osteogenic and chondrogenic differentiation

Bm-hMSCs were expanded and cell-encapsulating bioinks were prepared according to the methods described above. Then, 30 μL of each formulation was aliquoted into 3 mm diameter by 1 mm tall Teflon molds and fully crosslinked at 405 nm using the previously described energy dosage. Each sample was then individually placed into a 24-well plate and filled with 500 μL of either osteogenic medium, chondrogenic medium, or a 50:50 mixture of those two media. Chondrogenic medium was formulated as DMEM supplemented with 1% v/v ITS+ Premix (6.25 μg/mL insulin, 6.25 μg/mL transferrin, 6.25 μg/mL selenous acid, 5.35 μg/mL linoleic acid and 1.25 μg/mL bovine serum albumin), 50 mg/L ascorbic acid, 10^{-7} M dexamethasone, 10 ng/mL TGF-β3 with 1% w/v BSA as a carrier protein, and 1% v/v antibiotic-antimycotic [55,56]. Osteogenic medium was formulated as α-MEM supplemented with 10% v/v FBS, 50 mg/L ascorbic acid, 10^{-8} M dexamethasone, 10 mM β-glycerol 2-phosphate, and 1% v/v antibiotic-antimycotic [55,57]. Medium was exchanged 1 day after experiment initiation and then every 3–5 days afterwards, with the mixed media prepared immediately before exchanges. Acellular samples for every experimental group were included and subject to the same culturing conditions to control for any background signal that each formulation would cause in response to the biochemical assays below. For

the preliminary comparison of mineralization response between 10% w/v solutions of both SF-gelMA and DF-gelMA, samples were examined for DNA content and bound Ca^{2+} via Alizarin Red S staining using a plate reader according to kit instructions at 0, 14, and 28 days (n=4) [42]. Otherwise, samples were assessed in a separate experiment using only 10% w/v DF-gelMA at days 0, 7, 21, and 35 according to the following protocols (n=4).

2.9 Hydrogel homogenization for biochemical assays

Following each timepoint, all cell-encapsulating gel constructs were washed in PBS for 15 min at 37 °C and weighed for wet weight determination. Each was then placed into a polystyrene tube and frozen until characterization according to other hydrogel processing protocols [55,57,58]. Thawed samples were homogenized in 500 μL of sterile ultrapure H_2O using a Qiagen TissueLyser II (Hilden, Germany) at 30 s^{-1} for 5 min. A 60 μL aliquot of each suspension was diluted in a 1:1 volume ratio with 1 M acetic acid and incubated at room temperature for 16 hr to free Ca^{2+} ions for quantification using the Arsenazo III assay kit. The remaining 440 μL of homogenized sample suspension was diluted in a 1:1 volume ratio at 60 °C for 16 hr with an established digestion buffer containing 2 mg/mL proteinase K, 20 μg/mL pepstatin A, and 370 μg/mL iodoacetamide in tris–EDTA solution (12.11 mg/mL tris(hydroxymethyl aminomethane), 0.744 mg/mL EDTA, pH 7.6) to free DNA and sGAG content. The DNA and ECM content of the digested samples were then quantified using assay kits and the following protocols. Results were taken as two technical replicates to generate a mean value for each of the independent samples in each experimental group (n=4).

2.10 Biochemical assays of cell-encapsulating bioinks

DNA content was quantified using a Quant-iT PicoGreen dsDNA Assay Kit (Molecular Probes, Eugene, OR) and a plate reader (PowerWave x340 Microplate Reader; BioTek Instruments) following the manufacturer's instructions and recent methods [56]. Cell lysates were combined with the assay buffer and the PicoGreen dye solution within wells of an opaque 96-well assay plate and allowed to incubate for 10 min at room temperature. For sGAG deposition analysis, cell lysates were combined with DMMB color reagent at pH 1 within wells of a clear 96-well assay plate and quantified for absorbance at 520 nm [56]. GAG concentrations were determined relative to a chondroitin sulfate standard curve. The calcium content was quantified using a colorimetric Arsenazo III assay kit with 0–50 μg/mL Ca^{2+} as a standard curve [56]. Samples were combined with the kit reagent and the absorbance was measured at 650 nm. Due to the presence of β-TCP within the composite gels, samples had to be diluted 1:200 before assay application. All data for biochemical assays were subtracted by the acellular group signal within each assay, and then normalized to the wet weight of each individual sample. The experimental group average was then compared to that of both the day 0 values within each group and the control formulation of that cell culture medium condition in order to characterize both significant changes over time and significant effect of the bioink additive, respectively.

2.11 Histological analysis of sGAG presence in GAG-based bioinks

After 35 days of incubation within the mixed media and chondrogenic medium environments, both acellular and cell-laden HAMA-containing hydrogels were sectioned

and histologically stained, as outlined elsewhere [55,56]. Samples were fixed in 1 mL each of 10% neutral buffered formaldehyde for 24 hr at 37°C and then dehydrated in 1 mL of 70% ethanol for 24 hr at room temperature. Samples were then transferred to 10 × 10 × 15 mm cryomolds and immersed in optimal cutting temperature compound for 24 hr at 4 °C, followed by freezing overnight at −20°C. Samples were then processed on a Leica CM1850 cryotome (Wetzlar, Germany) to create 10 μm thick sections, mounted on glass slides, then dried and bound overnight at room temperature. Samples were rehydrated in 70% ethanol for 5 min. After tapping the slide dry, 6 N HCl was applied to samples for 30 s, tapped dry once more, and then pH 1 Alcian Blue stain was applied for 30 min. Following this, 6N HCl was applied dropwise via pipette for 20–30 s to de-stain, and then samples were washed for 5 min in running deionized water. The stained sections were then imaged using a Nikon Eclipse Ti2 (Tokyo, Japan) microscope at 20× magnification stitching a 6×6 field of view composite image, using 7 ms exposure and the brightfield auto-white setting at max LED intensity. Samples were then rehydrated in distilled water for 5–10 min, tapped dry, and covered with 10% v/v acetic acid for 5 min. Nuclear Fast Red stain was applied for 5 min, and then briefly de-stained with pipetted drops of the same acetic acid solution for 30 s and washed in deionized water for 5 min. After staining, samples were dehydrated in a standard graded ethanol to xylene wash, sealed with coverslips using Cytoseal XYL (Thomas Scientific, Swedesboro, NJ), and imaged via the same method.

2.12 Analysis of characteristic mRNA markers of hMSC osteogenic and chondrogenic differentiation via real time quantitative polymerase chain reaction (RT-qPCR)

The expression of 5 osteogenic and chondrogenic markers were evaluated according to similar RT-qPCR studies [55,56,59–61] (Table 1). To prepare samples for RNA extraction, hydrogels were washed in PBS for 15 min at 37°C, transferred to sterilized polystyrene tubes each containing a 5 mm stainless steel bead and 2 mL of RNAProtect reagent, and immediately frozen at −80°C until characterization. Within 30 days, samples were homogenized using a Qiagen TissueLyser II at 30 s^{-1} for 5 min and then centrifuged at 16,000*g for 5 min. The supernatant was aspirated, and then gel processing with gDNA and RNA columns was conducted according to RNEasy Mini Plus kit instructions.

For primer design, the NCBI primer designing tool was used (ncbi.nlm.nih.gov/tools/primer-blast/). Results from this tool were screened for amplicon length of ~100 bp or less and for their specificity using NCBI Standard Nucleotide BLAST (blast.ncbi.nlm.nih.gov). Primers are listed in Table 1 below and were purchased from IDT Technologies (Coralville, IA). To troubleshoot primer annealing temperature and quality of chosen primer sequences, 1 μg of RNA from control samples at 0 days of culture was reverse transcribed using an iScript cDNA Synthesis Kit and tested in a temperature gradient experiment from 50–60 °C, after which 58.3 °C was determined to be optimal based on melt curve analysis. For gene expression via RT-qPCR, 2 μL of a 1:10 dilution of cDNA was analyzed after being obtained according to the cDNA synthesis kit instructions with a final primer concentration of 500 nM. Day 7 and 35 samples were analyzed using the same primer concentration, but with 2 μL of undiluted cDNA to ensure robust gene expression profiles. RT-qPCR was completed using a CFX96 Touch Real-Time PCR Detection System within opaque white, skirted PCR plates (Bio-Rad, Hercules, CA). All C_q values were obtained automatically within Bio-Rad

CFX Maestro software. Gene expression was normalized to GAPDH expression at the same timepoint according to the $-2^{\Delta\Delta Cq}$ Livak method, shown below.

$$Normalized\ Expression\ Ratio = 2^{-\left(\left(Cq_{target,\ sample} - Cq_{GAPDH,\ sample}\right) - \left(Cq_{target,\ control} - Cq_{GAPDH,\ control}\right)\right)}$$

Negative control samples without the cDNA template were run in parallel to check for genomic DNA contamination, and melt-curve analyses were performed at the end of all PCR runs to ensure primer specificity [59]. Every RNA sample was analyzed using a Nanodrop ND-1000 Spectrophotometer (Thermo Scientific, Waltham, MA) and samples with a 260 nm/280 nm absorbance over 2.8 were considered contaminated and discarded as a quality control step (see Supp. Table 1). All groups were analyzed at n=3–4.

2.13 Rheological assessments of dynamic viscosity and shear-thinning response

To measure dynamic viscosity, samples were tested on a 40 mm parallel plate rheometer in flow mode [62]. Viscosity was taken as the average value from the stable, linear region after flow initiation during a 2 min experiment at 1 s^{-1} constant strain rate (n=3). Additionally, to assess the relationship between dynamic viscosity and shear rate, the input shear rate was ramped from 0.01 to 2000 s^{-1} (n=3).

2.14 Assessment of droplet surface tension and calculation of inkjet droplet Z-value

An CAM KSV goniometer/tensiometer (Ramé-Hart Instrument Co., New Jersey) was employed to measure the surface tension of bioink droplets that had been warmed above their gelation point (40 °C). The average surface tension value was measured for 2 min after 30 s of droplet stabilization and averaged per group (n=3). The Z-value, a dimensionless number correlating to droplet behavior, was then calculated using the following equation,

$$Z = \frac{1}{Oh} = \frac{\mathrm{Re}}{\sqrt{We}} = \frac{\sqrt{\gamma * \rho * a}}{\eta}$$

where γ is surface tension, η is dynamic viscosity, ρ is density, and a is the characteristic length [63,64]. For these bioinks, the density was assumed to be that of water, and the characteristic length of the droplet is the diameter of the nozzle opening, 100 μm. Dynamic viscosity measurements were gathered according to the method outlined above (n=3).

2.15 Bioprinting

2.15.1 Extrusion and inkjet printability trials—A Stratasys Fortus 450 (Eden Prairie, MN) was used to print the extrusion printability artifact that assessed the suitability of a bioink to overcome typical challenges in fabricating construct architecture, including layer stacking, tight angles, and bridging gaps [65]. All extrusion printing trials were performed with this artifact on a BioX (Cellink, Boston, MA). A speed of 2.5 mm/s was chosen for the tool head, and the minimum pressure that was able to extrude a given formulation was determined *via* the pressure testing printer function before each printing trial. For inkjet printing, a high-throughput assay was designed to quickly determine minimum valve cycle time and print pressure needed to deposit the smallest observed

continuous line of droplets was seen on the platform according to which obtained these values in a single print run (Supp. Fig. 4). All HAMA containing inks were printable at ambient temperature, and all β-TCP inks were printed at 35 °C to prevent ceramic particles clogging the nozzle. All HAMA inks and all inkjet trials were crosslinked with the printer 405 nm tool head between layers. For each extrusion print, all groups were binned into one of three qualitative categories based on the number of passed trials and the observed degree of printing uniformity (see Supp. Fig. 5).

2.15.2 DLP printability trials—All DLP printing was performed on a LumenX (Cellink, Boston, MA). The commercial UV absorber benzophenone-9 (R1800) was included at 0.5% w/v to block extraneous crosslinking outside of the region of exposed light. Since a very thorough analysis of this bioink additive was recently conducted showing the effects on DLP printability and *in vitro* biocompatibility, those investigations will not be repeated within this body of work [66]. Two assays were developed to understand the relationship between LAP:R1800 ratio and the resulting resolution of the printed construct. The first was a single-layer multi-exposure assay, similar to the original window pane tests used in early stereolithography [67], and the second was a *z*-resolution assay, where the effect of cumulative dosage over the length of the print can be better observed compared to the single-layer test (Supp. Fig. 6). For each ink formulation, the build platform was removed and 110 μL of ink was pipetted onto the build area and covered under a 50 × 22 mm glass slide to yield a 100 μm bioink layer. Then, at 10 mJ intervals the minimum dosage that crosslinked the bioink onto the glass slide was used as a starting point to tune the print process of the z-resolution assay construct. For the *z*-assay, 500 μL of ink was necessary for printing onto the build platform. From this multi-layer construct, the optimum energy within 50% of the dosage level observed to resolve the greatest number of open vertical and horizontal channels was then chosen to print the final construct, a 2 cm × 2 cm block with raised features in the shape of the Rice University logo. All constructs were designed in Autodesk Fusion 360 software (San Rafael, CA).

2.15.3 Bioprinting of cell-laden constructs and assessment of viable cells post-printing—hMSCs were expanded and encapsulated at 1 million cells/mL within each bioink according to the same methods described above. For all modalities, a 9 × 9 × 2 mm crosshatch design was used as the print file. Extrusion and inkjet constructs were printed using a 3D Discovery bioprinter within an enclosed, sterilizable biosafety cabinet (RegenHu, Villaz-St-Pierre, Switzerland). Constructs were printed in sterile conditions directly into a 12-well plate and exposed to 3 s of 1000 mW/cm^2 405 nm light between layers to fully crosslink all material. DLP constructs were individually placed into 12-well plates after a 1 min PBS wash. All samples received 1 mL of hMSC growth medium. Due to bioink opacity precluding optical viability stains, ATP content via a 3D culture-suited assay (CellTiter-3D Glo) was used to assess the relative cell proliferation via luminescence at 1 and 7 days after printing (n=4), read directly within each well. Non-printed, cellular bioink samples and acellular bioink samples were pipetted and crosslinked separately.

2.16 Presentation of data and statistical analyses

All data are presented as the mean with error bars representing one standard deviation from the mean unless otherwise indicated. Within each timepoint or media condition, two-way analysis of variance (ANOVA) was performed, followed by either a post-hoc Tukey's honestly significant difference (HSD) comparison of the mean for combinatorial experiments, displayed as a letter group, or by a Sidak's multiple comparisons test to individual assess the effect of time and treatment within the differentiation study. Differences are treated as statistically significant if the resulting p-value is less than 0.05. If two groups do not share a letter, they are significantly different. These analyses were performed in Prism 7.0 software (Graphpad Software, Inc., San Diego, CA) and JMP Pro 15 software (Cary, NC).

3. Results

3.1 Physicochemical comparison of base bioink gelMA polymers

To inform any observed differences in the biocompatibility data between the gelMA polymers, their physicochemical characteristics were examined, which is summarized in Fig. 1.

The GPC spectrograms shown in Fig. 1a indicate that even though the tail and peak size of the overall molecular weight distribution differed, both the number average and weight average molecular weights of each polymer as quantified by known PEG standards were within 3 kDa of each other, and the polydispersities of both gelMAs were between 1.2–1.3. The ^{1}H NMR data is shown in Fig. 1b. A higher total degree of methacrylation and methacryloylation was indicated by the relative integrals from three peaks present in the DF-gelMA spectra compared to that of the two peaks present in the methacryl region for the SF-gelMA. The control sample, a separately obtained porcine gelatin polymer, showed no peaks in this region. Confirmation of the DF-gelMA's higher degree of modification is seen in the significant reduction in the lysine peak, which is highest in the unmodified porcine gelatin control group.

Dynamic viscosity under constant shear and increasing shear rate were measured via continuous rheology experiments, summarized in Fig. 1c. The observed viscosity means dramatically changed for 20% w/v β-TCP level, but the difference was not significant. The inclusion of 20% β-TCP also led to significant decreases of the solutions' dynamic viscosity response to increasing shear rate. Using a power law correlation as given in previous extrusion bioprinting literature [62], the n-value exponent was extracted from the linear region of the shear sweep plot and used to quantify the shear thinning behavior. Both the 0% and 20% β-TCP levels possessed some degree of shear-thinning behavior (coefficient $n<1$), but differences were mainly attributed to β-TCP level, and there were also no significant differences between the SF- and DF-gelMA within each β-TCP level.

Using oscillatory photorheology, the UV-crosslinking of each methacryloylated polymer was examined, with the results shown in Fig. 1d. The DF-gelMA samples at both β-TCP levels had significantly higher crosslinked storage moduli than SF-gelMA samples, indicating that the DF-gelMA was more gel-like than the SF-gelMA, which matched the qualitative

handling of these gels by forceps shown in the right insets of Fig. 1e. Additionally, the DF-gelMA groups achieved 95% of their max storage moduli values more quickly than the SF-gelMA groups, taking 92 s compared to 216 s, and it was shown that the inclusion of 20 wt% β-TCP both significantly decreased the time it took to reach this point and increased the terminal storage moduli (Supp. Table 2).

After treating each gel with excess light to ensure full crosslinking has taken place, an enzyme-free PBS incubation study was initiated to understand the degree to which the composite gels lost mass in normal cell culture conditions over a 28-day period, since gelMAs with differing methacrylate and methacrylamide content have different hydrolytic stability [68]. The mass loss curves are summarized in Fig. 1e. The changes in lyophilized mass showed a significant decrease over time in the SF-gelMA samples within the first week of PBS incubation dropping to 14.1 ± 11.0% remaining mass on day 8, whereas the DF-gelMA samples' mass decreased on a much lower magnitude, dropping to 79.8 ± 3.14% remaining mass on day 8.

3.2 Effect of composite bioink components on cell viability, proliferation, and differentiation

The effects of both candidate gelMA polymers and the inclusion of the two tissue-specific additives, β-TCP and HAMA, on osteogenic and chondrogenic tissue-specific hMSC differentiation was studied by first characterizing the effects of each additive on cell viability and proliferation, which is summarized in Fig. 2.

First, the effect of novel bioink formulations on metabolic activity and viability of encapsulated hMSCs was assessed. Increasing HAMA content was shown to significantly decrease relative ATP content at 2 hr, but all 24 hr groups were similar to the control. No significant differences were observed with increasing HAMA in the cytotoxicity data assessed via dead cell DNA content. After troubleshooting a noted acidic effect using virgin β-TCP material, which is described in Supp. Fig. 3, a buffered version of the β-TCP reagent was characterized and used henceforth as the bone-specific additive within these studies. The encapsulated viability experiment showed differences in outcomes associated with gelMA polymer and β-TCP content. Combined, most SF- and DF-gelMA groups possessed viability greater than 50% at the 2 hr timepoint, including groups containing β-TCP. The percent of counted viable cells decreased in a dose-dependent manner relative to buffered β-TCP within each gelMA group regardless of gelMA source. The 10% DF-gelMA group showed a relative viability at 2 hr of greater than 90%. In the 2 hr timepoint, each 10% w/v SF-gelMA group showed a significantly lower mean compared to the 10% w/v DF-gelMA at the same β-TCP level. This trend of DF-gelMA possessing the relatively highest viability percentage continued into the 24 hr timepoint. Additionally, most groups for both the P- and DF-gelMA showed a significant decrease in viability percentage from 2 hr to 24 hr.

Comparisons of the two candidate gelMA polymers continued in a leachables experiment and an osteogenic differentiation study. Additionally, leachable compounds were specifically investigated to separate the viability effects that may arise from the shear stress-inducing process of encapsulation, summarized in Fig. 2b (left). After exposing leached compounds to cell monolayers, most groups possessed a % Live signal similar to or significantly

higher than the Live control groups at both the 2 hr and 24 hr timepoints. There were not any overarching significant trends within either the relationship between leachables media dilution and % Live signal or the comparisons made between P- and DF-gelMA at the same β-TCP level. From the % Dead signal data, all groups except the Dead control possessed a cytotoxic signal that was statistically similar to the Live controls at both timepoints ($p<0.05$).

A comparative, four-week osteogenic differentiation study was conducted to investigate the ability of these two gelMA polymers and buffered β-TCP to support calcium deposition, summarized in Fig. 2b (right). The highest DNA content was seen at day 0 for β-TCP-free DF-gelMA samples. Decreases in DNA content were associated with addition of β-TCP in both gelMA systems, and DNA content also decreased over time. Calcium deposition was noted over time in both ceramic-free gelMA samples. DF-gelMA had a higher Ca^{2+}-bound Alizarin Red S stain than SF-gelMA after 14 days and higher DNA content at days 0 and 14. After subtracting the acellular control groups' signals, no significant increases over time were noted in the β-TCP-containing groups.

Due to the double-functionalization of the DF-gelMA, its corresponding maintenance of crosslinked gel integrity over multi-week incubation periods, and its favorable viability and Ca^{2+} deposition outcomes, it was chosen as the base bioink backbone polymer for all following differentiation and printability studies

3.3. Tissue-specific ECM deposition of encapsulated hMSCs in novel bioink formulations

The β-TCP and HAMA additives were evaluated for their effects on the tissue-specific ECM deposition of 10% w/v DF-gelMA-encapsulated, differentiating hMSCs in tissue-specific and mixed cell culture media over a 35-day period, which is summarized in Fig. 3. A level of 0.5% w/v XG was included in all samples to prevent cell settling during hydrogel mold casting.

As shown in Fig. 3a, viable hMSC populations are maintained throughout the duration of the 35-day study. While most groups showed a significant decrease in DNA content with respect to their additive-free control in the same medium conditions, the mixed medium control group showed recovery and proliferation by the end of the study. The highest DNA content within all groups except for the mixed media control was seen at day 0.

The degree of mineralization via Ca^{2+} deposition is shown in shown in Fig. 3b. All groups containing the β-TCP showed significant Ca^{2+} deposition over time. The addition of 10% w/v β-TCP was shown to significantly increase the deposition of calcium in hMSCs by day 35 when compared to the additive-free control in the same osteogenic medium conditions. It is also notable that in the mixed 1:1 osteogenic:chondrogenic medium environment, bioink formulations with β-TCP showed statistically significant Ca^{2+} deposition over time relative to their respective day 0 groups, whereas all groups with HAMA did not.

Deposition data of a cartilage-like matrix through the synthesis and excretion of sulfated glycosaminoglycans (sGAGs) are shown in Fig. 3c. All groups containing HAMA showed significant increase in sGAG signals over time within separate media groups, indicating the support of sGAG deposition. The addition of 0.5% w/v HAMA was shown to significantly

increase the deposition of sGAGs in hMSCs by day 21 when compared to the additive-free control in the same mixed medium culturing conditions. Although the signals in most groups decreased by day 35, histological staining of these same samples with Alcian Blue indicated pericellular staining of sGAGs (see Supp. Figs. 7–9).

3.4 Effect of β-TCP and HAMA on osteogenic and chondrogenic markers of differentiation

Characteristic markers for osteogenic and chondrogenic differentiation were also examined over the duration of the differentiation study via RT-qPCR, which is summarized in Fig. 4.

In Figs. 4a and 4b, the results for two genetic markers often studied in osteogenic differentiation of hMSCs, RUNX2 and OCN, are shown. Within the RUNX2 expression data, the only significant difference was noted in the 0.5% w/v HAMA samples at Day 7 within the mixed media group, which was upregulated compared to the control. Within the OCN expression results, 10% w/v β-TCP, 0.5% w/v HAMA, and 2% w/v HAMA at day 35 in the mixed media group had relatively lower expression compared to the mixed media control at that timepoint. In Figs. 4c–4e, the results for three genetic markers often studied in chondrogenic differentiation of hMSCs, COL2A1, ACAN, and SOX9, are shown. In Fig. 4c, the same three groups which had significantly lower day 35 OCN expression, 10% w/v β-TCP, 0.5% w/v HAMA, and 2% w/v HAMA, showed signals indicating upregulation of COL2A1 at day 7, though these differences were not significant. Within the ACAN expression data in Fig. 4d, the same trends were observed as the COL2A1 data, where higher means were seen in some mixed media groups, but these differences were not significant. When analyzing SOX9 expression data shown in Fig. 4e, all groups containing HAMA had means at the day 7 timepoint which were higher than both their respective day 35 timepoint result and their respective medium control group, though not all comparisons were statistically significant. Only 0.5% and 2% w/v HAMA in the mixed medium condition significantly upregulated expression SOX9 compared to the control.

3.5 Effect of novel composite bioink components on responses to flow

After studying the effect of β-TCP and HAMA on the tissue-specific hMSC differentiation, these additives were studied for their effects on the shear-dependent dynamic viscosity. XG and NFC were also investigated as printability additives in these and following experiments, since a 37 °C bioink consisting of gelMA alone is above its melting temperature and therefore incapable of forming cohesive fibers or inkjet droplets that retain shape on the printing substrate. These results are summarized in Fig. 5.

In Figs. 5a and 5b, flow rheology experiments yielded dynamic viscosity data showing that concentrations of less than 2% w/v for both XG and NFC dramatically increases both the dynamic viscosity at low shear and the degree of shear-thinning in a dose-dependent manner. When including increasing concentrations of HAMA and β-TCP on these properties, shown in Figs. 5c and 5d, the highest additive levels increased nominal dynamic viscosity at the lowest assessed shear rates by a single order of magnitude.

3.6 Effect of printability additives on bioink printability outcomes

The concentrations of XG and NFC were studied for their effect on each bioprinting modality's printability. A summary of printing trials and formulations that resulted in the highest printability out of the tested groups, which are indicated by an asterisk, are shown in Fig. 6.

An extrusion printing artifact that subjects novel bioinks to a variety of tests including layer stacking, maintenance of open porosity, tight angles, and bridging gaps was chosen to qualitatively compare all bioinks. Results were binned into groups whose details are fully described in Supp. Fig. 5. As shown in Fig. 6a, increasing NFC to 2% led to formation of a more cohesive fiber, uniform printing, and more formulations passing extrusion print trials. Above the 1% XG level, however, viscosity was too high, and the printed fiber was either non-uniform or the maximum printer hardware pressure was exceeded for both the β-TCP and HAMA bioinks.

In Fig. 6b, constructs printed from XG-stabilized inkjet bioinks containing HAMA and β-TCP are shown. For inkjet printing, XG and gelMA concentration were tested for their effects on the Z-value, which is a measure of jetted droplet printability inversely proportional to dynamic viscosity [63,64]. Preliminary trials in gelatin solutions that included both XG and NFC yielded non-jettable bioink formulations, so NFC supplementation was excluded (Supp. Fig. 10). The highest levels of XG wt% led to the highest measured dynamic viscosities and therefore the lowest calculated Z-values, but due to the stabilization effect needed to prevent cell and ceramic settling given by at least 0.5% w/v XG presence in these gelMA bioinks, this 0.5% w/v XG level was chosen for future cell printing experiments (Supp. Fig. 11–12).

In Fig. 6c, constructs printed from XG-stabilized DLP bioinks containing HAMA and β-TCP are shown. Supplementation with a UV absorber was necessary to prevent extraneous crosslinking, and so addition of R1800 UV absorber along with the printer 405 nm light irradiance and intensity settings were studied (Supp. Fig. 6). Similar to the inkjet printing data, the addition of XG served to prevent ceramic and cell settling, though its addition here at 1% w/v was associated with damage to printed construct features due to viscosity-related suction forces inherent to how the platform raises and lowers into the bioink within an inverted DLP printing process (Supp. Fig. 13). For this same reason, XG alone was tested without NFC, as NFC was shown to even more dramatically increase solution viscosity at low weight percentages and would produce similar damage to the construct (Fig. 5). Constructs with 0.5% w/v XG both passed the qualitative printability trial by printing with intact features and could be removed and handled with integrity.

3.7 Cell-encapsulating extrusion, inkjet, and DLP bioprinting

To further characterize the formulations with the highest observed printability and assess the degree to which each ink supports cell growth and proliferation, hMSCs were encapsulated and printed within those bioinks, cultured in multi-well plates, and assayed for ATP content alongside pipetted, non-printed samples of each formulation up to seven days after printing, which is summarized in Fig. 7.

Extrusion- (Fig. 7a), inkjet- (Fig. 7b), and DLP-printed (Fig. 7c) crosshatch constructs measuring 9 mm × 9 mm × 2 mm and composed of either osteogenic or chondrogenic bm-hMSC-encapsulating bioinks were printed successfully. In the extrusion groups, the relatively lowest ATP concentration signals were observed. Among the inkjet groups, the pipetted bioink droplet samples showed an increase in ATP content when comparing day 1 data to day 7 data, but this change over time was not observed within the inkjet crosshatch constructs. The highest ATP content, which is directly correlated to cell number, was seen in the HAMA-containing constructs printed via DLP, which significantly increased ~2.4× from day 1 to day 7.

4. Discussion

A challenge within osteochondral tissue bioprinting is translating promising, biocompatible materials into bioink formulations that can fabricate constructs to further study questions in 3D space, including those interrogating architecture, spatial heterogeneity, and co-culture interactions. Here, we sought to document an approach to this process for two novel bioinks by first investigating the effects of gelMA, β-TCP, and HAMA on encapsulated cells' viability and osteochondral differentiation, then by studying the effect of printability additives XG and NFC on extrusion, inkjet, and DLP printability, and finally by bioprinting cell-laden constructs and examining the ATP content of viable encapsulated bm-hMSCs.

The untreated β-TCP ceramic material had a dramatic cytotoxic effect when used within cell-laden bioink cultures (Fig. 1). Once buffered, increasing β-TCP content significantly decreased encapsulated cell viability, but did not significantly affect leachables cytotoxicity. The use of DF-gelMA significantly increased the mineralization response of encapsulated hMSCs at the day 14 timepoint. SF-gelMA gels had lower integrity than those fabricated from DF-gelMA within the non-enzymatic PBS incubation study, and it also had less total methacryl content (Fig. 2). Using the DF-gelMA as the bioink base polymer for the comprehensive differentiation study, the presence of 10% w/v β-TCP increased the degree of matrix mineralization in mixed media conditions (Fig. 3). DNA content of all experimental groups decreased over time, with the largest decreases were seen in the samples that both contained β-TCP and had the highest reported mineralization data. Significant increases in the cartilage-specific sGAG content of all HAMA-containing bioinks were seen over time, and the presence of 0.5% w/v HAMA increased sGAG content relative to the control in mixed media conditions. Although β-TCP had significantly increased encapsulated cells' bone-like ECM deposition, this effect was not mirrored among data from mRNA markers of osteogenic differentiation at days 7 and 35 (Fig. 4). The presence of both 10% w/v β-TCP and HAMA decreased normalized expression of OCN at day 35 in the mixed media conditions. Among the investigated markers of chondrogenic differentiation in hMSCs, HAMA significantly upregulation SOX9 expression in both mixed media and chondrogenic medium conditions. It was also notable that the SOX9 upregulation caused by inclusion of 0.5% w/v HAMA in the mixed media conditions was corroborated by the ECM deposition data, where the same group also increased sGAG deposition relative to the control.

After completing the rheology and printability experiments, it was shown that inclusion of 2% w/v NFC increased the viscosity of solutions at low shear by four orders of magnitude

(Fig. 5). XG had a similar effect, increasing viscosity at lowest measured shear rate by three orders of magnitude. While the highest level of HAMA inclusion did not significantly alter viscosity, 20% w/v β-TCP was the observed threshold where viscosity increased by at least an order of magnitude, and also changed the slope of the shear-sweep data, indicating an increase in the degree of shear-thinning. These dramatic increases caused by the XG and NFC additives yielded printable extrusion and inkjet bioink formulations (Fig. 6). For DLP 3D printing, the inclusion of 0.5% w/v XG allowed for a stable suspension of ceramic particles to be printed in the 10% w/v β-TCP ink, and it also was able to print high-resolution features without damaging the printed construct during printing, unlike the 1% w/v XG formulations. Among all modalities, DLP printing yielded the highest number of viable cells via assessed ATP content (Fig. 7).

One of the strengths of these investigations is the combination of cell-encapsulating and monolayer viability experiments for examining the effect of CaP inclusion, since leachables viability experiments have a limitation where dead cells from the monolayer may wash away. A hypothesis that the shearing, physical interaction of ceramic particles affects cells to decrease viability can only be made after performing both experiments, and dilutions of leachables from buffered β-TCP did not affect exposed cells' Live or Dead signals while encapsulated viability decreased in a dose-dependent manner (Fig. 1). Additionally, another strength was seen in the 35-day differentiation study, which simultaneously investigated both the additives and the medium environment. This experimental structure allowed for separation of the effects of culture medium and bioink component on the measured biological outcomes, whose proposed mechanistic interpretations are outlined below. Since multiple cell lineages exist within the osteochondral unit, osteochondral tissue engineering studies often use a 1:1 mixture of osteogenic and chondrogenic medium as an experimental condition. Finally, by translating both the β-TCP- and HAMA-based bioinks individually into printable formulations for extrusion, inkjet, and DLP bioprinting, these experiments provide a flexible framework for the adaptation of other hydrogels into novel, printable bioinks that can be applied across common biofabrication strategies.

While the effect of CaP inclusion on compressive mechanical properties was measured separately (Supp. Fig. 14), the mechanical properties of every single bioink formulation were not recorded when assessing the effect of gelMA polymer, printability additives, or each bioprinter's crosslinking method and dosage. The addition of another functionalized polymer, HAMA, also likely changed the gelation, swelling, and mechanical properties, an effect shown in an experiment conducted to understand HAMA's differences swelling and compressive properties (Supp. Fig. 15). These particular mechanical measurements were outside of the scope of these studies, and while the aggregate effect of each variable can be seen in the results shown above, it is acknowledged that final matrix mechanical properties undoubtedly affect the responses of encapsulated MSCs, and that measurement of this bioink property would allow for a more well-rounded context for comparison to other cell-encapsulating gelMA hydrogels [69].

Previous studies utilizing β-TCP or similar CaPs within cell-laden hydrogels either obtain the commercially available material or synthesize the material *de novo* for experiments, and do not cite a similar acidic, cytotoxic acidic effect [40,42,47,70–77]. However, high-

concentration calcium phosphate cement studies have shown cell death in regions closest to the scaffold after seeding, which may be due to a phase transition followed by ion release of the ceramic material [18,78–80]. X-ray diffraction data indicated that the β-TCP studied here did not change phase within the week where the majority of cell death occurred (Supp. Fig. 16). The results of the initial cell-encapsulation experiment also align with studies investigating bioactive glasses, where the material must be pre-conditioned before the resulting ion-release and suspension pH are sufficiently biocompatible for *in vitro* cell culture since sudden changes in osmotic pressure and pH are cytotoxic [81]. Similarly, by performing both a cell-encapsulating and a monolayer leachables experiment with β-TCP composite bioink gels, the PBS conditioning process was demonstrated to sufficiently buffer the CaP material and allow for moderate cell viability within the gels (Fig. 1). The decreases in viability associated with increasing buffered β-TCP content likely arise from both the increased non-hydrogel mass within the solution and increased viscosity (Fig. 5). Even though these solutions possess shear-thinning properties (Fig 5.), any cytotoxic shear forces potentially induced by the positive displacement pipette mixing method, which was needed to prevent aggregation and adequately disperse cells, could have increased cell death [82]. This explanation is corroborated by the fact that in the leachables experiment with the same β-TCP formulations, where cells were not mixed or encapsulated, non-diluted aliquots of the leached content yielded no significant differences in Live or Dead signals of exposed cells (Fig. 1). Still, it was noted that more cell death was observed at the periphery of the bioink droplet cultures (Supp. Fig. 1). This may be due to the higher degree of free radical generation from the dissolved LAP photoinitiator at the edges of the droplet closest to the crosslinking light. The wavelength used, 405 nm, is safer then UV light for *in vitro* cell studies, but can still be cytotoxic [83,84].

While each gelMA was similar in molecular weight, the ^{1}H NMR spectra and photorheology data clearly explain some of their difference in outcome from the incubation experiment. The three peaks present in the DF-gelMA ^{1}H NMR spectra indicate a higher degree of methacryl functionalization, often due to an additional methacryloylation step in the synthesis of the material [24]. Comparing these results to other studies utilizing gelMA backbones in hydrogel or bioink systems that also performed ^{1}H NMR analyses, a single-functionalized gelMA polymer material appears to be more common [1,21,85–89]. The DF-gelMA's increased density of reactive sites likely caused the stiffer, more gel-like properties of the DF-gelMA indicated by photorheology, and this stiffness could have encouraged the upregulated calcium deposition noted at day 14, a phenomenon observed in other similar studies [71,90–92].

The decline in DNA content over time was observed in both the 28-day gelMA osteogenic differentiation study and the 35-day comprehensive differentiation study (Fig. 1d). While both these data may indicate some degree of cell death after initial encapsulation, it must be noted that Ca^{2+} ions and DNA molecules have opposite charges and may possess a significant affinity toward each other. This explanation is supported by an experiment varying the sampling method of digested gels where, within the samples containing β-TCP, the reported DNA content dropped when sampling only the supernatant (Supp. Fig. 17). Homogeneous sampling was used for all data presented here, but this still demonstrates that DNA may have more affinity for the CaP particles and mineralized hydrogel than

the fluorescent probe, causing an artifact where reported DNA content decreases and that the assay is under-reporting the samples. In addition to this interaction, other studies investigating the osteogenic differentiation of MSCs over month-long periods also report that the proliferation of cells is significantly decreased or that DNA content decreases in differentiating MSC populations [55,93].

The presence of 10% w/v β-TCP significantly increasing matrix mineralization in mixed media conditions but not osteogenic medium conditions may indicate the importance of TGFβ−3 growth factor triggering hMSCs' mineralization response, a bioactive factor included in the chondrogenic medium due to its previously noted chondrogenic effects [94–100]. The β-TCP-laden gelMA may have resembled the mineralized collagen environment of native bone and caused osteoblast-like behavior within the hMSCs. Calcium phosphates like β-TCP support osteoblast-like differentiation within osteogenic cell culture conditions due to their ability to sequester growth factors, provide surface area, and provide inorganic elements necessary for mineralization [19,47,101].

Even though increases in sGAG content were noted over time in the HAMA groups, the overall trends of sGAG presence were lower than expected in spite of HyAc's well-characterized effects on upregulating markers of chondrogenesis in MSCs [102–107]. Histological staining of these samples with Nuclear Fast Red and Alcian Blue at pH 1 for sulfated GAGs revealed perinuclear blue staining at the day 35 timepoint, which supports the biochemical assay data (Supp. Figs. 7–9). It is possible that sGAGs were leached out from the hydrogels over time, which has been noted elsewhere [105,108].

β-TCP upregulated mineralization, but its presence did not significantly upregulate the investigated osteogenic mRNA markers. Despite this, when interpreting these and other RT-qPCR data alongside the ECM deposition data, the increased means of the early markers RUNX2 and SOX9 can help explain the increases in sGAG and Ca^{2+} deposition within the mixed media environment samples, which were significant increases relative to the cellular control and after acellular sample signal subtraction. RUNX2 is a transcription factor for earlymid stage differentiation of hMSCs into osteoblastic lineage, and OCN is a transcription factor associated with osteocalcin production, which is secreted in late stages of osteogenic differentiation [109–112]. Notably, this was the group with the highest reported mineralization, and much like the observed affinity between DNA and Ca^{2+}, negatively-charged RNA may also have similar interactions with calcium phosphate-containing or highly mineralized hydrogel samples. HAMA's downregulation of OCN is a phenomenon noted in chondrogenic differentiation studies [40]. Still, HAMA has been noted elsewhere to upregulate OCN expression and other osteogenic markers, and its role and mechanisms within osteogenesis is not fully understood [113–115]. Mixed media HAMA groups also had nominal calcium deposition signals higher than that of the chondrogenic medium groups, and so the same aforementioned hypothesis of deposited calcium interfering with assays for genetic material may apply here. All HAMA-containing groups possessed group means of upregulated SOX9 expression both greater than their day 35 data and respective medium condition controls, however only the mixed media comparisons were statistically significant. SOX9 is a gene the encodes the transcription factor of the same name which plays a key role in early-/mid-stage differentiation

into chondrocytic lineages for hMSCs [116,117]. When studied *in vitro* with stem cell cultures, crosslinked HAMA hydrogels have been shown to interact with CD44 receptors of stem cells and possess mechanical properties similar to a cartilage microenvironment, including elastic modulus, which both influence stem cell differentiation into chondrocytes [102,103,106].

There are two notes of additional context when interpreting this data relative to other biomaterials' effects on differentiating stem cells. Firstly, all the experiments described herein, aside from assessing the toxicity of leachable molecules, were examined in a cell-encapsulating 3D culture environment, which can change cells' responses to external stimuli when compared to their 2D culture [118–120]. Secondly, much of what has been previously reported in the literature utilizes cells from strain-controlled species chosen for their suitability for *in vitro* and *in vivo* studies, including that of rabbits, rats, pigs, or mice. Stem cell species affects measured responses within *in vitro* culture environments [121–123]. The human-sourced cell within this study were screened by the manufacturer for cell surface antigens that indicate 'stemness', and they were also tested for their tri-lineage differentiation (see 2.1 Materials). Additionally, they were derived from a female donor, and previous studies have noted differences in biological outcomes when studying the same type of stem cells among different donors and different sexes [124–127]. This lack of cell source diversity is a limitation of these studies. However, these hMSCs were acquired from a reputable source that fully characterizes their donor lots for markers of stemness and the ability to differentiate into multiple lineages (see Supp. Table 3 for additional information about the hMSC lot characteristics). Also, it should be noted that while the candidate primer sequences were verified using Day 0 samples of the same hMSC populations, the lack of positive controls for the RT-qPCR analyses is a limitation of these studies.

Both printability additives, NFC and XG, significantly increased viscosity. NFC is well characterized for its effect on solution viscosity due to the aggregation of nanometer-scale features and fragments of well-dispersed cellulose material [25–28]. XG had a similar effect, increasing viscosity at low shear by three orders of magnitude. Employed for this effect within the food industry, branched chains of xanthan gum entangle and aggregate at low percentages [29–32]. While the highest level of HAMA inclusion did not significantly alter viscosity, 20% w/v β-TCP was the observed threshold where viscosity increased by at least an order of magnitude, and also changed the slope of the shear-sweep data, indicating a change in the degree of shear-thinning. Within this group, a critical concentration of ceramic particles is reached where gel-like properties dominate and the solution does not flow at rest (Supp. Fig. 18). After examining the printability data with this contextual rheological data (Fig. 6), it can be understood that XG and NFC impart a tunability to a bioink's rheological properties that affects its qualitative printing outcomes, but past certain concentration levels, such as above 1% w/v XG for extrusion bioinks, the additives' combined dose-dependent effects on viscosity made the gelMA solutions too viscous to print uniformly or without damaging the constructs.

Printability has recently been defined as the ability of a material to be printed in a way which results in printing outcomes which are desirable for a given application when subjected to a certain set of printing conditions [128]. For these experiments, the printing

conditions are the limitations of pressure, speed, or light exposure inherent by the printer within each printing modality, and the desirable outcome is the ability to resolve features of 100 – 500 μm, which is comparable to state-of-the-art 3D printing systems [129]. The increases in viscosity supplemented also by the increase in degree of shear-thinning provided by the additives helped not only form cohesive fibers and droplets that did not spread on the glass substrates, but also flowed smoothly when subject to sufficient extruding pressures (Supp. Fig. 5). Additionally, the interaction effect between the positively charged β-TCP particles and the anionic xanthan gum polymeric chains may have increased viscosity [1,72]. For DLP printing, the NFC additive was not added to formulations because its more dramatic effect on increasing viscosity is detrimental to the DLP printing process, which relies on free fluid movement to re-coat the build area with non-crosslinked photopolymer for the next layer. β-TCP- and HAMA-containing formulations were each assessed for their printability using a university logo-based trial with the dye kept at a cytocompatible level of 0.5% w/v [66]. The 100 μm resolution features of the β-TCP ink is on the order of scaffold resolution found in other recent examples of DLP printing with calcium phosphates for bone-tissue engineering applications [130–136]. The print accuracy decreased after including the ceramic material, which can be explained both by the light-scattering effect of particulate additives like β-TCP as well as its previously noted effect on increasing crosslinking kinetics (Fig. 2) [137,138]. The 100 μm resolution for the HAMA bioink is comparable to other HAMA-containing DLP bioinks [44,139,140]. Xanthan gum was included to prevent cell and ceramic settling, and this also increased the ability to manipulate the crosslinked gels without fracture (not shown), which was not possible in HAMA gels that did not have the XG additive. HyAc is a polymer with molecular weights in the millions of Da, so replacing the shorter gelMA polymer backbone with this longer-chain polymer may increase the elasticity of the crosslinked construct [102].

The cell-encapsulating bioprinting experiments showed that DLP printing yielded constructs with the highest normalized ATP content (Fig. 7), which has been verified previously with bone marrow-derived hMSCs and is directly proportional to the number of viable cells and amount of double-stranded DNA within a sample [46,141]. One difference in formulation is the inclusion of NFC for the extrusion inks, which was shown to dramatically increase viscosity by several orders of magnitude. Examining only the printed scaffold groups, this result of DLP inks displaying a superior number of viable cells compares favorably to other evaluations of printing methods which state that, due to the lack of a nozzle and lower viscosity requirements, shear forces are present within DLP printing at a level much lower than that of extrusion and inkjet printing, contributing to higher cell survival [1,82,142].

Comparisons among the pipetted samples across modalities can be made to separate any confounding effects of each individual 3D printing method. The inkjet and DLP formulations only differed in the inclusion of the UV absorber for DLP bioinks, which has a noted dose-dependent cytotoxicity that may explain a lack of observed proliferation in the DLP pipetted groups [66]. For all extrusion groups, the additional inclusion of 2% w/v NFC gave these inks the relatively highest solid material content and greater dynamic viscosity and gel-like rheological properties, which can increase the imparted shear forces under flow conditions [143,144]. Increasing NFC content in a hydrogel network is associated with decreasing its swelling ratio [145]. This change in the network’s water uptake likely created

a difference in the ability of the ATP reporter assay to penetrate the network to encapsulated cells within the construct, potentially resulting in the relatively low observed signals [146]. Elsewhere, NFC has been used successfully as a viable bioink material and characterized extensively within other biocompatible hydrogel systems using stains and microscopy techniques that were not utilized here, since the relatively high concentration (≥10% w/v) of the calcium phosphate additive imparted a high opacity and also autofluoresces in the red channel commonly used for fluorescent stains [1,27,143,145,147]. Other methods of cell quantification, such as the DNA assay used in the differentiation studies, were considered for measuring proliferation, although as previously noted, there is an interaction between the DNA and the β-TCP included in half of the printable bioinks as well as the fluorescent background issue, and constructs on the centimeter scale included considerably more calcium phosphate than the gels used in the differentiation studies. The additional additives also significantly blocked transmitted light needed for Live/Dead staining (see Supp. Fig. 19). These background signal and affinity limitations were not observed with the ATP luminescent reporter assay.

5. Conclusions

In these studies, we investigated the effect of β-TCP and HAMA on the viability and differentiation of encapsulated hMSCs within novel gelMA-based composite bioinks, and then examined NFC and XG additives and new methods that facilitated their cell-encapsulating bioprinting. The DF-gelMA material was shown to be associated with significantly higher hMSC viability, mineralization, and gel stability compared to SF-gelMA, which was attributed to a higher degree of methacryl functionalization. Incorporation of 10% w/v β-TCP significantly increased the hMSC mineralization response within a mixed osteogenic and chondrogenic culture medium environment, though significant upregulation of osteogenic markers RUNX2 and OCN were not observed. The inclusion of HAMA was associated with increased sGAG deposition over time in mixed and chondrogenic media, significantly higher sGAG deposition in mixed media, and HAMA also significantly upregulated expression of RUNX2 and SOX9 within mixed media. The late-stage expression of OCN was decreased in both β-TCP and HAMA-containing bioinks in mixed media. The dose-dependent increases in dynamic viscosity, shear-thinning properties, and crosslinked integrity of bioinks from inclusion of XG and NFC facilitated the deposition of uniform extrusion fibers, the formation of cohesive jetted droplets, and the construction of intact photocrosslinked constructs within extrusion, inkjet, and DLP 3D printing modalities, respectively. Among the formulations with the optimal observed printability within each method, HAMA-containing DLP bioink formulations yielded the highest number of viable cells. Using these six printable bioink formulations, future studies can interrogate other relationships between bioink component additives and outcomes important for osteochondral tissue engineering studies, such as the effect of printability additives concentration and the bioinks' crosslinked mechanical properties, or the implications of multi-material scaffold architectures. In summary, the characterization of these novel bioinks and the chronicling of their print processes provide a platform for the adaptation of novel hydrogel systems into a library of printable bioinks and modular

additives, capable of fabricating tissue-specific constructs *via* the three most common bioprinting modalities across multiple bioprinting devices.

Supplementary Material

Refer to Web version on PubMed Central for supplementary material.

Acknowledgements

The authors would like to acknowledge support from the National Institutes of Health (P41 EB023833), the National Science Foundation Graduate Research Fellowship Program (MLB), National Institute of Dental and Craniofacial Research (F31 DE030333, KJH), the Baylor College of Medicine Medical Science Training Program (KJH), and the Rice University Sustaining Excellence in Research Scholars Program (ALT). The authors would like to thank Humabiologics, Inc. for providing discounted human-derived gelMA, and other Industry Collaborators within the Regenerative Medicine Development Organization (ReMDO) and the Wake Forest Institute for Regenerative Medicine for providing research equipment and resources. Funding is provided by the Medical Technology Enterprise Consortium (MTEC) via the U.S. Army Medical Research and Development Command (USAMRDC). The views and conclusions contained herein are those of the authors and should not be interpreted as necessarily representing the official policies or endorsements, either expressed or implied, by the U.S. Government. Microscopy was conducted using resources of the Shared Equipment Authority at Rice University within the Bioscience Research Collaborative. Dr. Jane Grande-Allen is acknowledged for use of plate reader and RT-qPCR thermocycler.

8. References

[1]. Bedell ML, Navara AM, Du Y, Zhang S and Mikos AG 2020 Polymeric Systems for Bioprinting Chem. Rev 120 10744–92 [PubMed: 32469510]

[2]. Suh S, Shin J, Kim J, Kim J, Beak C, Kim D-I, Kim H, Jeon S and Choo I-W 2002 Effect of Different Particles on Cell Proliferation in Polymer Scaffolds Using a Solvent-Casting and Particulate Leaching Technique Asaio Journal 48 460–4 [PubMed: 12296562]

[3]. Harris LD, Kim B-S and Mooney DJ 1998 Open pore biodegradable matrices formed with gas foaming Journal of Biomedical Materials Research 42 396–402 [PubMed: 9788501]

[4]. Buchko CJ, Chen LC, Shen Y and Martin DC 1999 Processing and microstructural characterization of porous biocompatible protein polymer thin films Polymer 40 7397–407

[5]. Boland ED, Wnek GE, Simpson DG, Pawlowski KJ and Bowlin GL 2001 Tailoring Tissue Engineering Scaffolds Using Electrostatic Processing Techniques: A Study of Poly(glycolic Acid) Electrospinning Journal of Macromolecular Science, Part A 38 1231–43

[6]. Tibbitt MW and Anseth KS 2009 Hydrogels as Extracellular Matrix Mimics for 3D Cell Culture Biotechnol Bioeng 103 655–63 [PubMed: 19472329]

[7]. Miao S, Zhu W, Castro NJ, Leng J and Zhang LG 2016 Four-Dimensional Printing Hierarchy Scaffolds with Highly Biocompatible Smart Polymers for Tissue Engineering Applications Tissue Eng Part C Methods 22 952–63 [PubMed: 28195832]

[8]. Du Y, Guo JL, Wang J, Mikos AG and Zhang S 2019 Hierarchically designed bone scaffolds: From internal cues to external stimuli Biomaterials 218 119334

[9]. Camarero-Espinosa S, Rothen-Rutishauser B, Foster EJ and Weder C 2016 Articular cartilage: from formation to tissue engineering Biomater. Sci 4 734–67 [PubMed: 26923076]

[10]. Temenoff JS and Mikos AG 2000 Review: tissue engineering for regeneration of articular cartilage Biomaterials 21 431–40 [PubMed: 10674807]

[11]. Kim E, Guilak F and Haider MA 2008 The Dynamic Mechanical Environment of the Chondrocyte: A Biphasic Finite Element Model of Cell-Matrix Interactions Under Cyclic Compressive Loading J Biomech Eng 130

[12]. Garg HG and Hales CA 2004 Chemistry and Biology of Hyaluronan (Elsevier)

[13]. Necas J, Bartosikova L, Brauner P and Kolar J 2008 Hyaluronic acid (hyaluronan): a review Veterinarni Medicina 53 397–411

[14]. Khan Y, Yaszemski MJ, Mikos AG and Laurencin CT 2008 Tissue Engineering of Bone: Material and Matrix Considerations JBJS 90 36

[15]. Diaz-Gomez LA, Smith BT, Kontoyiannis PD, Bittner SM, Melchiorri AJ and Mikos AG 2018 Multimaterial segmented fiber printing for gradient tissue engineering Tissue Engineering Part C: Methods

[16]. Bittner SM, Guo JL, Melchiorri A and Mikos AG 2018 Three-dimensional printing of multilayered tissue engineering scaffolds Materials Today 21 861–74 [PubMed: 30450010]

[17]. Bittner SM, Smith BT, Diaz-Gomez L, Hudgins CD, Melchiorri AJ, Scott DW, Fisher JP and Mikos AG 2019 Fabrication and mechanical characterization of 3D printed vertical uniform and gradient scaffolds for bone and osteochondral tissue engineering Acta Biomaterialia 90 37–48 [PubMed: 30905862]

[18]. Ahlfeld T, Doberenz F, Kilian D, Vater C, Korn P, Lauer G, Lode A and Gelinsky M 2018 Bioprinting of mineralized constructs utilizing multichannel plotting of a self-setting calcium phosphate cement and a cell-laden bioink Biofabrication 10 045002

[19]. LeGeros RZ 2008 Calcium Phosphate-Based Osteoinductive Materials Chem. Rev. 108 4742–53

[20]. Ogose A, Hotta T, Kawashima H, Kondo N, Gu W, Kamura T and Endo N 2005 Comparison of hydroxyapatite and beta tricalcium phosphate as bone substitutes after excision of bone tumors Journal of Biomedical Materials Research Part B: Applied Biomaterials 72B 94–101

[21]. Nichol JW, Koshy S, Bae H, Hwang CM, Yamanlar S and Khademhosseini A 2010 Cell-laden microengineered gelatin methacrylate hydrogels Biomaterials 31 5536–44 [PubMed: 20417964]

[22]. Yue K, Trujillo-de Santiago G, Alvarez MM, Tamayol A, Annabi N and Khademhosseini A 2015 Synthesis, properties, and biomedical applications of gelatin methacryloyl (GelMA) hydrogels Biomaterials 73 254–71 [PubMed: 26414409]

[23]. Yue K, Li X, Schrobback K, Sheikhi A, Annabi N, Leijten J, Zhang W, Zhang YS, Hutmacher DW, Klein TJ and Khademhosseini A 2017 Structural analysis of photocrosslinkable methacryloyl-modified protein derivatives Biomaterials 139 163–71 [PubMed: 28618346]

[24]. Claaßen C, Claaßen MH, Truffault V, Sewald L, Tovar GEM, Borchers K and Southan A 2018 Quantification of Substitution of Gelatin Methacryloyl: Best Practice and Current Pitfalls Biomacromolecules 19 42–52 [PubMed: 29211461]

[25]. Khan RA, Salmieri S, Dussault D, Uribe-Calderon J, Kamal MR, Safrany A and Lacroix M 2010 Production and Properties of Nanocellulose-Reinforced Methylcellulose-Based Biodegradable Films J. Agric. Food Chem. 58 7878–85

[26]. Sultan S, Siqueira G, Zimmermann T and Mathew AP 2017 3D printing of nano-cellulosic biomaterials for medical applications Current Opinion in Biomedical Engineering 2 29–34

[27]. Markstedt K, Mantas A, Tournier I, Ávila HM, Hägg D and Gatenholm P 2015 3D Bioprinting Human Chondrocytes with Nanocellulose–Alginate Bioink for Cartilage Tissue Engineering Applications

[28]. Möller T, Amoroso M, Hägg D, Brantsing C, Rotter N, Apelgren P, Lindahl A, Kölby L and Gatenholm P 2017 In Vivo Chondrogenesis in 3D Bioprinted Human Cell-laden Hydrogel Constructs Plast Reconstr Surg Glob Open 5 e1227

[29]. Kumar A, Rao KM and Han SS 2018 Application of xanthan gum as polysaccharide in tissue engineering: A review Carbohydrate Polymers 180 128–44 [PubMed: 29103488]

[30]. Rochefort WE and Middleman S 1987 Rheology of Xanthan Gum: Salt, Temperature, and Strain Effects in Oscillatory and Steady Shear Experiments Journal of Rheology 31 337–69

[31]. Song K-W, Kim Y-S and Chang G-S 2006 Rheology of concentrated xanthan gum solutions: Steady shear flow behavior Fibers Polym 7 129–38

[32]. Zhong L, Oostrom M, Truex MJ, Vermeul VR and Szecsody JE 2013 Rheological behavior of xanthan gum solution related to shear thinning fluid delivery for subsurface remediation Journal of Hazardous Materials 244–245 160–70

[33]. Murphy SV and Atala A 2014 3D bioprinting of tissues and organs Nature Biotechnology 32 773–85

[34]. Panwar A and Tan LP 2016 Current Status of Bioinks for Micro-Extrusion-Based 3D Bioprinting Molecules 21

[35]. Carrow JK, Kerativitayanan P, Jaiswal MK, Lokhande G and Gaharwar AK 2015 Chapter 13 - Polymers for Bioprinting Essentials of 3D Biofabrication and Translation ed A Atala and J J Yoo (Boston: Academic Press) pp 229–48

[36]. Mendes AC, Baran ET, Pereira RC, Azevedo HS and Reis RL 2012 Encapsulation and Survival of a Chondrocyte Cell Line within Xanthan Gum Derivative Macromolecular Bioscience 12 350–9 [PubMed: 22213743]

[37]. Kumar A, Rao KM, Kwon SE, Lee YN and Han SS 2017 Xanthan gum/bioactive silica glass hybrid scaffolds reinforced with cellulose nanocrystals: Morphological, mechanical and in vitro cytocompatibility study Materials Letters 193 274–8

[38]. Petta D, D'Amora U, Ambrosio L, Grijpma DW, Eglin D and D'Este M 2020 Hyaluronic acid as a bioink for extrusion-based 3D printing Biofabrication 12 032001

[39]. Kumar A, Matari IAI and Han SS 2020 3D printable carboxylated cellulose nanocrystal-reinforced hydrogel inks for tissue engineering Biofabrication 12 025029

[40]. Kosik-Koziol A, Costantini M, Mróz A, Idaszek J, Heljak M, Jaroszewicz J, Kijeńska E, Szöke K, Frerker N, Barbetta A, Brinchmann JE and Święszkowski W 2019 3D bioprinted hydrogel model incorporating beta-tricalcium phosphate for calcified cartilage tissue engineering Biofabrication 11 035016

[41]. Liu J, Li L, Suo H, Yan M, Yin J and Fu J 2019 3D printing of biomimetic multi-layered GelMA/nHA scaffold for osteochondral defect repair Materials & Design 171 107708

[42]. Kim W and Kim G 2019 Collagen/bioceramic-based composite bioink to fabricate a porous 3D hASCs-laden structure for bone tissue regeneration Biofabrication 12 015007

[43]. Pepelanova I, Kruppa K, Scheper T and Lavrentieva A 2018 Gelatin-Methacryloyl (GelMA) Hydrogels with Defined Degree of Functionalization as a Versatile Toolkit for 3D Cell Culture and Extrusion Bioprinting Bioengineering 5 55

[44]. Lam T, Dehne T, Krüger JP, Hondke S, Endres M, Thomas A, Lauster R, Sittinger M and Kloke L 2019 Photopolymerizable gelatin and hyaluronic acid for stereolithographic 3D bioprinting of tissue-engineered cartilage Journal of Biomedical Materials Research Part B: Applied Biomaterials 107 2649–57 [PubMed: 30860678]

[45]. Skardal A 2018 Perspective: "Universal" bioink technology for advancing extrusion bioprinting-based biomanufacturing Bioprinting 10 e00026

[46]. Bedell ML, Melchiorri AJ, Aleman J, Skardal A and Mikos AG 2020 A high-throughput approach to compare the biocompatibility of candidate bioink formulations Bioprinting 17 e00068

[47]. Wenz A, Borchers K, Tovar GEM and Kluger PJ 2017 Bone matrix production in hydroxyapatite-modified hydrogels suitable for bone bioprinting Biofabrication 9 044103

[48]. Vo TN, Ekenseair AK, Kasper FK and Mikos AG 2014 Synthesis, Physicochemical Characterization, and Cytocompatibility of Bioresorbable, Dual-Gelling Injectable Hydrogels Biomacromolecules 15 132–42 [PubMed: 24320599]

[49]. Masuelli MA 2014 Mark-Houwink Parameters for Aqueous-Soluble Polymers and Biopolymers at Various Temperatures Journal of Polymer and Biopolymer Physics Chemistry 2 37–43

[50]. Kim YS, Guo JL, Lam J, Grande-Allen KJ, Engel PS and Mikos AG 2019 Synthesis of Injectable, Thermally Responsive, Chondroitin Sulfate-Cross-Linked Poly(N-isopropylacrylamide) Hydrogels ACS Biomater. Sci. Eng 5 6405–13

[51]. Van Hoorick J, Gruber P, Markovic M, Tromayer M, Van Erps J, Thienpont H, Liska R, Ovsianikov A, Dubruel P and Van Vlierberghe S 2017 Cross-Linkable Gelatins with Superior Mechanical Properties Through Carboxylic Acid Modification: Increasing the Two-Photon Polymerization Potential Biomacromolecules 18 3260–72 [PubMed: 28850786]

[52]. Barth HG, Provder T and Urban MW 2001 Chromatographic Characterization of Polymers: Hyphenated and Multidimensional Techniques (American Chemical Society)

[53]. Veis A 1964 The macromolecular chemistry of gelatin (New York, N.Y: Academic Press, Inc.)

[54]. Quero F, Padilla C, Campos V, Luengo J, Caballero L, Melo F, Li Q, Eichhorn SJ and Enrione J 2018 Stress transfer and matrix-cohesive fracture mechanism in microfibrillated cellulose-gelatin nanocomposite films Carbohydrate Polymers 195 89–98 [PubMed: 29805028]

[55]. Guo JL, Li A, Kim YS, Xie VY, Smith BT, Watson E, Bao G and Mikos AG 2019 Click functionalized, tissue-specific hydrogels for osteochondral tissue engineering Journal of Biomedical Materials Research Part A 108 684–93 [PubMed: 31755226]

[56]. Lam J, Clark EC, Fong ELS, Lee EJ, Lu S, Tabata Y and Mikos AG 2016 Evaluation of cell-laden polyelectrolyte hydrogels incorporating poly(l-Lysine) for applications in cartilage tissue engineering Biomaterials 83 332–46 [PubMed: 26799859]

[57]. Vo TN, Tabata Y and Mikos AG 2016 Effects of cellular parameters on the in vitro osteogenic potential of dual-gelling mesenchymal stem cell-laden hydrogels Journal of Biomaterials Science, Polymer Edition 27 1277–90 [PubMed: 27328947]

[58]. Lu S, Lee EJ, Lam J, Tabata Y and Mikos AG 2016 Evaluation of Gelatin Microparticles as Adherent-Substrates for Mesenchymal Stem Cells in a Hydrogel Composite Ann Biomed Eng 44 1894–907 [PubMed: 26935924]

[59]. Anderson JM, Vines JB, Patterson JL, Chen H, Javed A and Jun H-W 2011 Osteogenic Differentiation of Human Mesenchymal Stem Cells Synergistically Enhanced by Biomimetic Peptide Amphiphiles Combined with Conditioned Media Acta Biomater 7 675–82 [PubMed: 20728586]

[60]. Schilling T, Nöth U, Klein-Hitpass L, Jakob F and Schütze N 2007 Plasticity in adipogenesis and osteogenesis of human mesenchymal stem cells Molecular and Cellular Endocrinology 271 1–17 [PubMed: 17475397]

[61]. Xu J, Wang W, Ludeman M, Cheng K, Hayami T, Lotz JC and Kapila S 2008 Chondrogenic Differentiation of Human Mesenchymal Stem Cells in Three-Dimensional Alginate Gels Tissue Engineering Part A 14 667–80 [PubMed: 18377198]

[62]. Paxton N, Smolan W, Böck T, Melchels F, Groll J and Jungst T 2017 Proposal to assess printability of bioinks for extrusion-based bioprinting and evaluation of rheological properties governing bioprintability Biofabrication 9 044107

[63]. Negro A, Cherbuin T and Lutolf MP 2018 3D Inkjet Printing of Complex, Cell-Laden Hydrogel Structures Sci Rep 8 17099 [PubMed: 30459444]

[64]. Derby B 2010 Inkjet Printing of Functional and Structural Materials: Fluid Property Requirements, Feature Stability, and Resolution Annual Review of Materials Research 40 395–414

[65]. Uzun-Per M, Gillispie GJ, Tavolara TE, Yoo JJ, Atala A, Gurcan MN, Lee SJ and Niazi MKK 2021 Automated Image Analysis Methodologies to Compute Bioink Printability Advanced Engineering Materials 23 2000900

[66]. Huh J, Moon Y-W, Park J, Atala A, Yoo JJ and Lee SJ 2021 Combinations of photoinitiator and UV absorber for cell-based digital light processing (DLP) bioprinting Biofabrication 13 034103

[67]. Jacobs PF 1992 Rapid Prototyping & Manufacturing: Fundamentals of Stereolithography (Society of Manufacturing Engineers)

[68]. Zheng J, Zhu M, Ferracci G, Cho N-J and Lee BH 2018 Hydrolytic Stability of Methacrylamide and Methacrylate in Gelatin Methacryloyl and Decoupling of Gelatin Methacrylamide from Gelatin Methacryloyl through Hydrolysis Macromolecular Chemistry and Physics 219 1800266

[69]. Freeman FE and Kelly DJ 2017 Tuning Alginate Bioink Stiffness and Composition for Controlled Growth Factor Delivery and to Spatially Direct MSC Fate within Bioprinted Tissues Scientific Reports 7 17042 [PubMed: 29213126]

[70]. You F, Chen X, Cooper DML, Chang T and Eames BF 2018 Homogeneous hydroxyapatite/alginate composite hydrogel promotes calcified cartilage matrix deposition with potential for three-dimensional bioprinting Biofabrication 11 015015

[71]. Marques CF, Diogo GS, Pina S, Oliveira JM, Silva TH and Reis RL 2019 Collagen-based bioinks for hard tissue engineering applications: a comprehensive review J Mater Sci: Mater Med 30 32 [PubMed: 30840132]

[72]. Heid S and Boccaccini AR 2020 Advancing bioinks for 3D bioprinting using reactive fillers: A review Acta Biomaterialia 113 1–22 [PubMed: 32622053]

[73]. De Mori A, Peña Fernández M, Blunn G, Tozzi G and Roldo M 2018 3D Printing and Electrospinning of Composite Hydrogels for Cartilage and Bone Tissue Engineering Polymers 10 285

[74]. Demirtaş TT, Irmak G and Gümüşderelioğlu M 2017 A bioprintable form of chitosan hydrogel for bone tissue engineering Biofabrication 9 035003

[75]. Trombetta R, Inzana JA, Schwarz EM, Kates SL and Awad HA 2017 3D Printing of Calcium Phosphate Ceramics for Bone Tissue Engineering and Drug Delivery Ann Biomed Eng 45 23–44 [PubMed: 27324800]

[76]. Wang X-F, Lu P-J, Song Y, Sun Y-C, Wang Y-G and Wang Y 2016 Nano hydroxyapatite particles promote osteogenesis in a three-dimensional bio-printing construct consisting of alginate/gelatin/hASCs RSC Advances 6 6832–42

[77]. Bendtsen ST, Quinnell SP and Wei M 2017 Development of a novel alginate-polyvinyl alcohol-hydroxyapatite hydrogel for 3D bioprinting bone tissue engineered scaffolds Journal of Biomedical Materials Research Part A 105 1457–68 [PubMed: 28187519]

[78]. Graham S and Brown PW 1993 The low temperature formation of octacalcium phosphate Journal of Crystal Growth 132 215–25

[79]. Anada T, Sato T, Kamoya T, Shiwaku Y, Tsuchiya K, Takano-Yamamoto T, Sasaki K and Suzuki O 2016 Evaluation of bioactivity of octacalcium phosphate using osteoblastic cell aggregates on a spheroid culture device Regenerative Therapy 3 58–62 [PubMed: 31245473]

[80]. Kamakura S, Sasano Y, Shimizu T, Hatori K, Suzuki O, Kagayama M and Motegi K 2002 Implanted octacalcium phosphate is more resorbable than β-tricalcium phosphate and hydroxyapatite Journal of Biomedical Materials Research 59 29–34 [PubMed: 11745534]

[81]. Ciraldo FE, Boccardi E, Melli V, Westhauser F and Boccaccini AR 2018 Tackling bioactive glass excessive in vitro bioreactivity: Preconditioning approaches for cell culture tests Acta Biomaterialia 75 3–10 [PubMed: 29772346]

[82]. Blaeser A, Campos DFD, Puster U, Richtering W, Stevens MM and Fischer H 2016 Controlling Shear Stress in 3D Bioprinting is a Key Factor to Balance Printing Resolution and Stem Cell Integrity Advanced Healthcare Materials 5 326–33 [PubMed: 26626828]

[83]. Pahoff S, Meinert C, Bas O, Nguyen LJ, Klein TW and Hutmacher D 2019 Effect of gelatin source and photoinitiator type on chondrocyte redifferentiation in gelatin methacryloyl-based tissue-engineered cartilage constructs Journal of Materials Chemistry B 7 1761–72 [PubMed: 32254918]

[84]. Nguyen AK, Goering PL, Elespuru RK, Sarkar Das S and Narayan RJ 2020 The Photoinitiator Lithium Phenyl (2,4,6-Trimethylbenzoyl) Phosphinate with Exposure to 405 nm Light Is Cytotoxic to Mammalian Cells but Not Mutagenic in Bacterial Reverse Mutation Assays Polymers 12 1489

[85]. Erdem A, Darabi MA, Nasiri R, Sangabathuni S, Ertas YN, Alem H, Hosseini V, Shamloo A, Nasr AS, Ahadian S, Dokmeci MR, Khademhosseini A and Ashammakhi N 2020 3D Bioprinting of Oxygenated Cell-Laden Gelatin Methacryloyl Constructs Advanced Healthcare Materials 9 1901794

[86]. Schuurman W, Levett PA, Pot MW, Weeren PR van Dhert WJA, Hutmacher DW, Melchels FPW, Klein TJ and Malda J 2013 Gelatin-Methacrylamide Hydrogels as Potential Biomaterials for Fabrication of Tissue-Engineered Cartilage Constructs Macromolecular Bioscience 13 551–61 [PubMed: 23420700]

[87]. Ying G, Jiang N, Yu C and Zhang YS 2018 Three-dimensional bioprinting of gelatin methacryloyl (GelMA) Bio-des. Manuf. 1 215–24

[88]. Chen Y-C, Lin R-Z, Qi H, Yang Y, Bae H, Melero-Martin JM and Khademhosseini A 2012 Functional Human Vascular Network Generated in Photocrosslinkable Gelatin Methacrylate Hydrogels Advanced Functional Materials 22 2027–39 [PubMed: 22907987]

[89]. Hutson CB, Nichol JW, Aubin H, Bae H, Yamanlar S, Al-Haque S, Koshy ST and Khademhosseini A 2011 Synthesis and Characterization of Tunable Poly(Ethylene Glycol): Gelatin Methacrylate Composite Hydrogels Tissue Engineering Part A 17 1713–23 [PubMed: 21306293]

[90]. Pek YS, Wan ACA and Ying JY 2010 The effect of matrix stiffness on mesenchymal stem cell differentiation in a 3D thixotropic gel Biomaterials 31 385–91

[91]. Lee J, Jeon O, Kong M, Abdeen AA, Shin J-Y, Lee HN, Lee YB, Sun W, Bandaru P, Alt DS, Lee K, Kim H-J, Lee SJ, Chaterji S, Shin SR, Alsberg E and Khademhosseini A 2020

Combinatorial screening of biochemical and physical signals for phenotypic regulation of stem cell–based cartilage tissue engineering Science Advances 6 eaaz5913

[92]. Vining KH and Mooney DJ 2017 Mechanical forces direct stem cell behaviour in development and regeneration Nat Rev Mol Cell Biol 18 728–42 [PubMed: 29115301]

[93]. Korn P, Ahlfeld T, Lahmeyer F, Kilian D, Sembdner P, Stelzer R, Pradel W, Franke A, Rauner M, Range U, Stadlinger B, Lode A, Lauer G and Gelinsky M 2020 3D Printing of Bone Grafts for Cleft Alveolar Osteoplasty – In vivo Evaluation in a Preclinical Model Front. Bioeng. Biotechnol 8

[94]. Schneider MC, Chu S, Randolph MA and Bryant SJ 2019 An in vitro and in vivo comparison of cartilage growth in chondrocyte-laden matrix metalloproteinase-sensitive poly(ethylene glycol) hydrogels with localized transforming growth factor β3 Acta Biomaterialia 93 97–110

[95]. Cho H, Lee A and Kim K 2018 The effect of serum types on Chondrogenic differentiation of adipose-derived stem cells Biomaterials Research 22 6 [PubMed: 29556415]

[96]. Yang Q, Teng B-H, Wang L-N, Li K, Xu C, Ma X-L, Zhang Y, Kong D-L, Wang L-Y and Zhao Y-H 2017 Silk fibroin/cartilage extracellular matrix scaffolds with sequential delivery of TGF-β3 for chondrogenic differentiation of adipose-derived stem cells Int J Nanomedicine 12 6721–33

[97]. Dahlin RL, Ni M, Meretoja VV, Kasper FK and Mikos AG 2014 TGF-β3-induced chondrogenesis in co-cultures of chondrocytes and mesenchymal stem cells on biodegradable scaffolds Biomaterials 35 123–32 [PubMed: 24125773]

[98]. Mueller MB, Fischer M, Zellner J, Berner A, Dienstknecht T, Prantl L, Kujat R, Nerlich M, Tuan RS and Angele P 2010 Hypertrophy in Mesenchymal Stem Cell Chondrogenesis: Effect of TGF-β Isoforms and Chondrogenic Conditioning CTO 192 158–66 [PubMed: 20407224]

[99]. Guo X, Liao J, Park H, Saraf A, Raphael RM, Tabata Y, Kasper FK and Mikos AG 2010 Effects of TGF-β3 and preculture period of osteogenic cells on the chondrogenic differentiation of rabbit marrow mesenchymal stem cells encapsulated in a bilayered hydrogel composite Acta Biomaterialia 6 2920–31

[100]. Shen B, Wei A, Tao H, Diwan AD and Ma DDF 2008 BMP-2 Enhances TGF-β3– Mediated Chondrogenic Differentiation of Human Bone Marrow Multipotent Mesenchymal Stromal Cells in Alginate Bead Culture Tissue Engineering Part A 15 1311–20

[101]. LeGeros RZ, Lin S, Rohanizadeh R, Mijares D and LeGeros JP 2003 Biphasic calcium phosphate bioceramics: preparation, properties and applications Journal of Materials Science: Materials in Medicine 14 201–9

[102]. Allison DD and Grande-Allen KJ 2006 Review. Hyaluronan: A Powerful Tissue Engineering Tool Tissue Engineering 12 2131–40 [PubMed: 16968154]

[103]. Wu S-C, Chen C-H, Chang J-K, Fu Y-C, Wang C-K, Eswaramoorthy R, Lin Y-S, Wang Y-H, Lin S-Y, Wang G-J and Ho M-L 2013 Hyaluronan initiates chondrogenesis mainly via CD44 in human adipose-derived stem cells Journal of Applied Physiology 114 1610–8 [PubMed: 23449937]

[104]. Bian L, Guvendiren M, Mauck RL and Burdick JA 2013 Hydrogels that mimic developmentally relevant matrix and N-cadherin interactions enhance MSC chondrogenesis PNAS 110 10117–22 [PubMed: 23733927]

[105]. Erickson IE, Huang AH, Sengupta S, Kestle S, Burdick JA and Mauck RL 2009 Macromer density influences mesenchymal stem cell chondrogenesis and maturation in photocrosslinked hyaluronic acid hydrogels Osteoarthritis and Cartilage 17 1639–48 [PubMed: 19631307]

[106]. Burdick JA and Prestwich GD 2011 Hyaluronic Acid Hydrogels for Biomedical Applications Advanced Materials 23 H41–56 [PubMed: 21394792]

[107]. Camci-Unal G, Cuttica D, Annabi N, Demarchi D and Khademhosseini A 2013 Synthesis and Characterization of Hybrid Hyaluronic Acid-Gelatin Hydrogels Biomacromolecules 14 1085–92 [PubMed: 23419055]

[108]. Kim YS, Chien AJ, Guo JL, Smith BT, Watson E, Pearce HA, Koons GL, Navara AM, Lam J, Scott DW, Grande-Allen KJ and Mikos AG 2020 Chondrogenesis of cocultures of mesenchymal stem cells and articular chondrocytes in poly(l-lysine)-loaded hydrogels Journal of Controlled Release 328 710–21 [PubMed: 33010336]

[109]. Blair HC, Larrouture QC, Li Y, Lin H, Beer-Stoltz D, Liu L, Tuan RS, Robinson LJ, Schlesinger PH and Nelson DJ 2016 Osteoblast Differentiation and Bone Matrix Formation In Vivo and In Vitro Tissue Engineering Part B: Reviews 23 268–80 [PubMed: 27846781]

[110]. Tian X-F, Heng B-C, Ge Z, Lu K, Rufaihah AJ, Fan VT-W, Yeo J-F and Cao T 2008 Comparison of osteogenesis of human embryonic stem cells within 2D and 3D culture systems Scandinavian Journal of Clinical and Laboratory Investigation 68 58–67

[111]. Takahashi Y, Yamamoto M and Tabata Y 2005 Osteogenic differentiation of mesenchymal stem cells in biodegradable sponges composed of gelatin and beta-tricalcium phosphate Biomaterials 26 3587–96 [PubMed: 15621249]

[112]. Kim K, Dean D, Lu A, Mikos AG and Fisher JP 2011 Early osteogenic signal expression of rat bone marrow stromal cells is influenced by both hydroxyapatite nanoparticle content and initial cell seeding density in biodegradable nanocomposite scaffolds Acta Biomater 7 1249–64 [PubMed: 21074640]

[113]. Mathews S, Mathew SA, Gupta PK, Bhonde R and Totey S 2014 Glycosaminoglycans enhance osteoblast differentiation of bone marrow derived human mesenchymal stem cells Journal of Tissue Engineering and Regenerative Medicine 8 143–52 [PubMed: 22499338]

[114]. Haghjoo M, Azarbayjani MA, Peeri M and Hosseini SA 2019 Effect of Training, Hyaluronic Acid, and Mesenchymal Stem Cell Therapies on Osteocalcin Gene Expression in Cartilage Tissue of Rats with Knee Osteoarthritis Gene Cell Tissue 6

[115]. Kawano M, Ariyoshi W, Iwanaga K, Okinaga T, Habu M, Yoshioka I, Tominaga K and Nishihara T 2011 Mechanism involved in enhancement of osteoblast differentiation by hyaluronic acid Biochemical and Biophysical Research Communications 405 575–80 [PubMed: 21266161]

[116]. Bi W, Deng JM, Zhang Z, Behringer RR and de Crombrugghe B 1999 Sox9 is required for cartilage formation Nature Genetics 22 85–9 [PubMed: 10319868]

[117]. de Crombrugghe B, Lefebvre V, Behringer RR, Bi W, Murakami S and Huang W 2000 Transcriptional mechanisms of chondrocyte differentiation Matrix Biology 19 389–94 [PubMed: 10980415]

[118]. Bellas E and Chen CS 2014 Forms, forces, and stem cell fate Current Opinion in Cell Biology 31 92–7 [PubMed: 25269668]

[119]. Molina ER, Chim LK, Salazar MC, Mehta SM, Menegaz BA, Lamhamedi-Cherradi S-E, Satish T, Mohiuddin S, McCall D, Zaske AM, Cuglievan B, Lazar AJ, Scott DW, Grande-Allen JK, Ludwig JA and Mikos AG 2019 Mechanically tunable coaxial electrospun models of YAP/TAZ mechanoresponse and IGF-1R activation in osteosarcoma Acta Biomaterialia 100 38–51 [PubMed: 31542501]

[120]. Molina ER, Chim LK, Salazar MC, Koons GL, Menegaz BA, Ruiz-Velasco A, Lamhamedi-Cherradi S-E, Vetter AM, Satish T, Cuglievan B, Smoak MM, Scott DW, Ludwig JA and Mikos AG 2020 3D Tissue-Engineered Tumor Model for Ewing's Sarcoma That Incorporates Bone-like ECM and Mineralization ACS Biomater. Sci. Eng 6 539–52

[121]. Ren G, Su J, Zhang L, Zhao X, Ling W, L'huillie A, Zhang J, Lu Y, Roberts AI, Ji W, Zhang H, Rabson AB and Shi Y 2009 Species Variation in the Mechanisms of Mesenchymal Stem Cell-Mediated Immunosuppression STEM CELLS 27 1954–62 [PubMed: 19544427]

[122]. Schnerch A, Cerdan C and Bhatia M 2010 Distinguishing Between Mouse and Human Pluripotent Stem Cell Regulation: The Best Laid Plans of Mice and Men STEM CELLS 28 419–30 [PubMed: 20054863]

[123]. Wei CL, Miura T, Robson P, Lim S-K, Xu X-Q, Lee MY-C, Gupta S, Stanton L, Luo Y, Schmitt J, Thies S, Wang W, Khrebtukova I, Zhou D, Liu ET, Ruan YJ, Rao M and Lim B 2005 Transcriptome Profiling of Human and Murine ESCs Identifies Divergent Paths Required to Maintain the Stem Cell State STEM CELLS 23 166–85 [PubMed: 15671141]

[124]. Vancamp P, Gothié J-D, Luongo C, Sébillot A, Le Blay K, Butruille L, Pagnin M, Richardson SJ, Demeneix BA and Remaud S 2019 Gender-specific effects of transthyretin on neural stem cell fate in the subventricular zone of the adult mouse Sci Rep 9 19689 [PubMed: 31873158]

[125]. Kim M, Erickson IE, Huang AH, Garrity ST, Mauck RL and Steinberg DR 2018 Donor Variation and Optimization of Human Mesenchymal Stem Cell Chondrogenesis in Hyaluronic Acid Tissue Engineering Part A 24 1693–703 [PubMed: 29792383]

[126]. Tajiri N, Duncan K, Borlongan MC, Pabon M, Acosta S, De la Pena I, Hernadez-Ontiveros D, Lozano D, Aguirre D, Reyes S, Sanberg PR, Eve DJ, Borlongan CV and Kaneko Y 2014 Adult Stem Cell Transplantation: Is Gender a Factor in Stemness? International Journal of Molecular Sciences 15 15225–43 [PubMed: 25170809]

[127]. Herrmann JL, Abarbanell AM, Weil BR, Manukyan MC, Poynter JA, Wang Y, Coffey AC and Meldrum DR 2010 Gender Dimorphisms in Progenitor and Stem Cell Function in Cardiovascular Disease J. of Cardiovasc. Trans. Res 3 103–13

[128]. Gillispie G, Prim P, Copus J, Fisher J, Mikos AG, Yoo JJ, Atala A and Lee SJ 2020 Assessment methodologies for extrusion-based bioink printability Biofabrication 12 022003

[129]. Kang H-W, Lee SJ, Ko IK, Kengla C, Yoo JJ and Atala A 2016 A 3D bioprinting system to produce human-scale tissue constructs with structural integrity Nature Biotechnology 34 312–9

[130]. Kim J-W, Yang B-E, Hong S-J, Choi H-G, Byeon S-J, Lim H-K, Chung S-M, Lee J-H and Byun S-H 2020 Bone Regeneration Capability of 3D Printed Ceramic Scaffolds International Journal of Molecular Sciences 21 4837

[131]. Liu S, Mo L, Bi G, Chen S, Yan D, Yang J, Jia Y-G and Ren L 2021 DLP 3D printing porous β-tricalcium phosphate scaffold by the use of acrylate/ceramic composite slurry Ceramics International 47 21108–16

[132]. Wu Y, Chen X, Zhao G, Chen R, Liu Y, Ren H, Qu X and Liu Y 2019 β-Tricalcium phosphate/ε-polycaprolactone composite scaffolds with a controllable gradient: Fabrication and characterization Ceramics International 45 16188–94

[133]. Liu S, Chen J, Chen T and Zeng Y 2021 Fabrication of trabecular-like beta-tricalcium phosphate biomimetic scaffolds for bone tissue engineering Ceramics International 47 13187–98

[134]. Lim H-K, Hong S-J, Byeon S-J, Chung S-M, On S-W, Yang B-E, Lee J-H and Byun S-H 2020 3D-Printed Ceramic Bone Scaffolds with Variable Pore Architectures International Journal of Molecular Sciences 21 6942

[135]. Xu S, Zhang H, Li X, Zhang X, Liu H, Xiong Y, Gao R and Yu S 2021 Fabrication and biological evaluation of porous β-TCP bioceramics produced using digital light processing Proc Inst Mech Eng H 09544119211041186

[136]. Cho YS, Yang S, Choi E, Kim KH and Gwak S-J 2021 Fabrication of a porous hydroxyapatite scaffold with enhanced human osteoblast-like cell response via digital light processing system and biomimetic mineralization Ceramics International 47 35134–43

[137]. Mott EJ, Busso M, Luo X, Dolder C, Wang MO, Fisher JP and Dean D 2016 Digital micromirror device (DMD)-based 3D printing of poly(propylene fumarate) scaffolds Materials Science and Engineering: C 61 301–11 [PubMed: 26838854]

[138]. Wallace J, Wang MO, Thompson P, Busso M, Belle V, Mammoser N, Kim K, Fisher JP, Siblani A, Xu Y, Welter JF, Lennon DP, Sun J, Caplan AI and Dean D 2014 Validating continuous digital light processing (cDLP) additive manufacturing accuracy and tissue engineering utility of a dye-initiator package Biofabrication 6 015003

[139]. Hossain Rakin R 2020 Development of a hyaluronic acid-based hybrid bioink for stereolithography 3D bioprinting (University of British Columbia)

[140]. Zhou F, Hong Y, Liang R, Zhang X, Liao Y, Jiang D, Zhang J, Sheng Z, Xie C, Peng Z, Zhuang X, Bunpetch V, Zou Y, Huang W, Zhang Q, Alakpa EV, Zhang S and Ouyang H 2020 Rapid printing of bio-inspired 3D tissue constructs for skin regeneration Biomaterials 258 120287

[141]. Dominijanni AJ, Devarasetty M, Forsythe SD, Votanopoulos KI and Soker S 2021 Cell Viability Assays in Three-Dimensional Hydrogels: A Comparative Study of Accuracy Tissue Engineering Part C: Methods 27 401–10 [PubMed: 34082602]

[142]. Grigoryan B, Paulsen SJ, Corbett DC, Sazer DW, Fortin CL, Zaita AJ, Greenfield PT, Calafat NJ, Gounley JP, Ta AH, Johansson F, Randles A, Rosenkrantz JE, Louis-Rosenberg JD, Galie PA, Stevens KR and Miller JS 2019 Multivascular networks and functional intravascular topologies within biocompatible hydrogels Science 364 458–64 [PubMed: 31048486]

[143]. Pääkkö M, Ankerfors M, Kosonen H, Nykänen A, Ahola S, Österberg M, Ruokolainen J, Laine J, Larsson PT, Ikkala O and Lindström T 2007 Enzymatic Hydrolysis Combined with Mechanical Shearing and High-Pressure Homogenization for Nanoscale Cellulose Fibrils and Strong Gels Biomacromolecules 8 1934–41 [PubMed: 17474776]

[144]. Nair SS, Zhu JY, Deng Y and Ragauskas AJ 2014 Hydrogels Prepared from Cross-Linked Nanofibrillated Cellulose ACS Sustainable Chem. Eng. 2 772–80

[145]. Borges AC, Eyholzer C, Duc F, Bourban P-E, Tingaut P, Zimmermann T, Pioletti DP and Månson J-AE 2011 Nanofibrillated cellulose composite hydrogel for the replacement of the nucleus pulposus Acta Biomaterialia 7 3412–21 [PubMed: 21651996]

[146]. Liu Y and Chan-Park MB 2009 Hydrogel based on interpenetrating polymer networks of dextran and gelatin for vascular tissue engineering Biomaterials 30 196–207 [PubMed: 18922573]

[147]. Apelgren P, Amoroso M, Lindahl A, Brantsing C, Rotter N, Gatenholm P and Kölby L 2017 Chondrocytes and stem cells in 3D-bioprinted structures create human cartilage in vivo PLOS ONE 12 e0189428

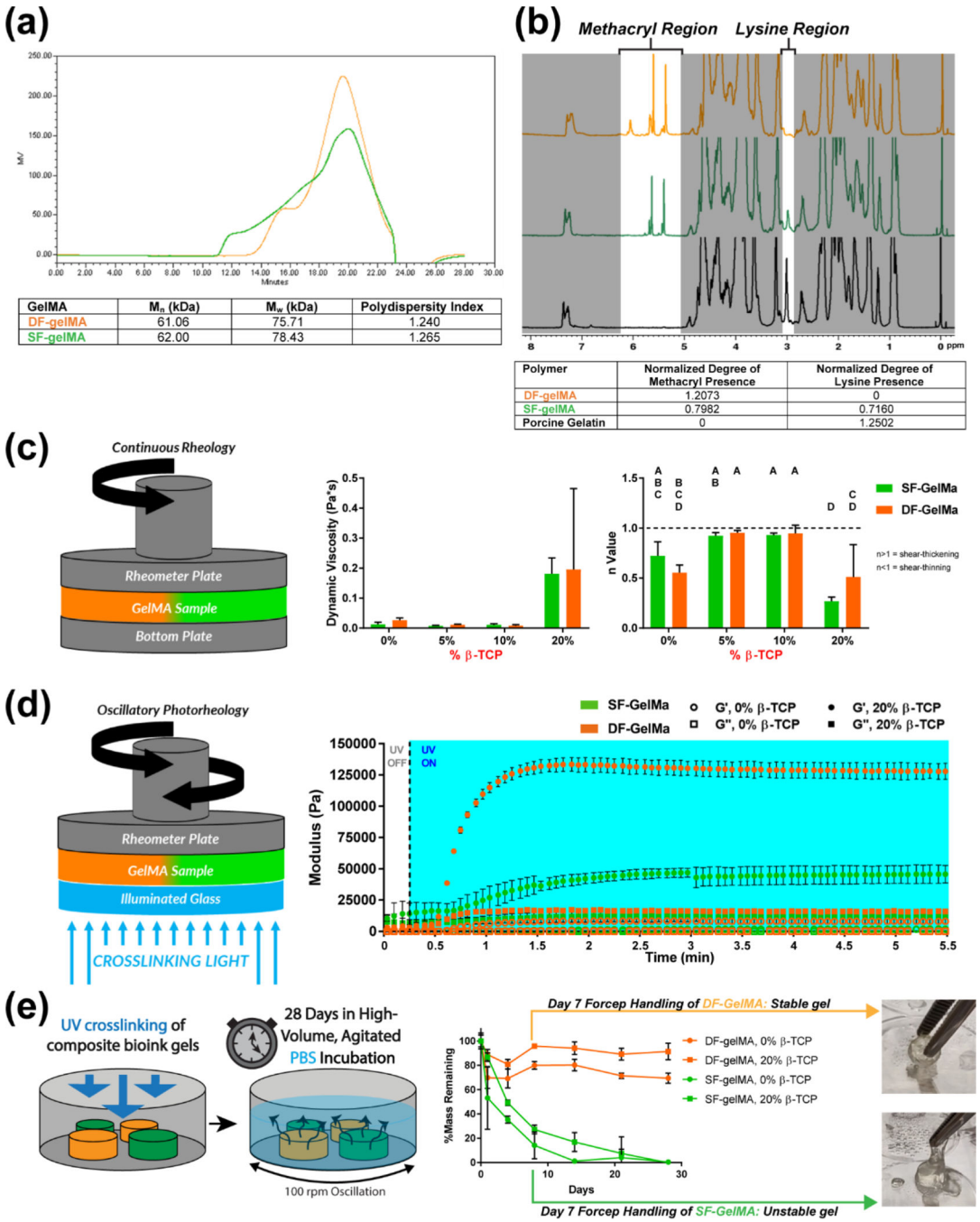

GelMA	M_n (kDa)	M_w (kDa)	Polydispersity Index
DF-gelMA	61.06	75.71	1.240
SF-gelMA	62.00	78.43	1.265

Polymer	Normalized Degree of Methacryl Presence	Normalized Degree of Lysine Presence
DF-gelMA	1.2073	0
SF-gelMA	0.7982	0.7160
Porcine Gelatin	0	1.2502

Figure 1.

(**a**) Aqueous GPC spectrograms with quantified molecular weight for P- and DF-gelMA polymers. (**b**) ^{1}H NMR data comparing unmodified porcine gelatin, SF-gelMA, and DF-gelMA with methacryl and lysine data normalized to each polymer's respective phenylalanine region integral (7.2–7.5 ppm). (**c**) Rheological data comparing 10% w/v P- and DF-gelMA polymer solutions. (**d**) Photorheological data displaying the moduli during UV crosslinking of 10% w/v P- and DF-gelMA polymer solutions. (e) Mass loss data from a

4-week PBS incubation study, along with images depicting relative loss or retention of initial gel crosslinking at day 7 for samples fabricated from each gelMA polymer backbone.

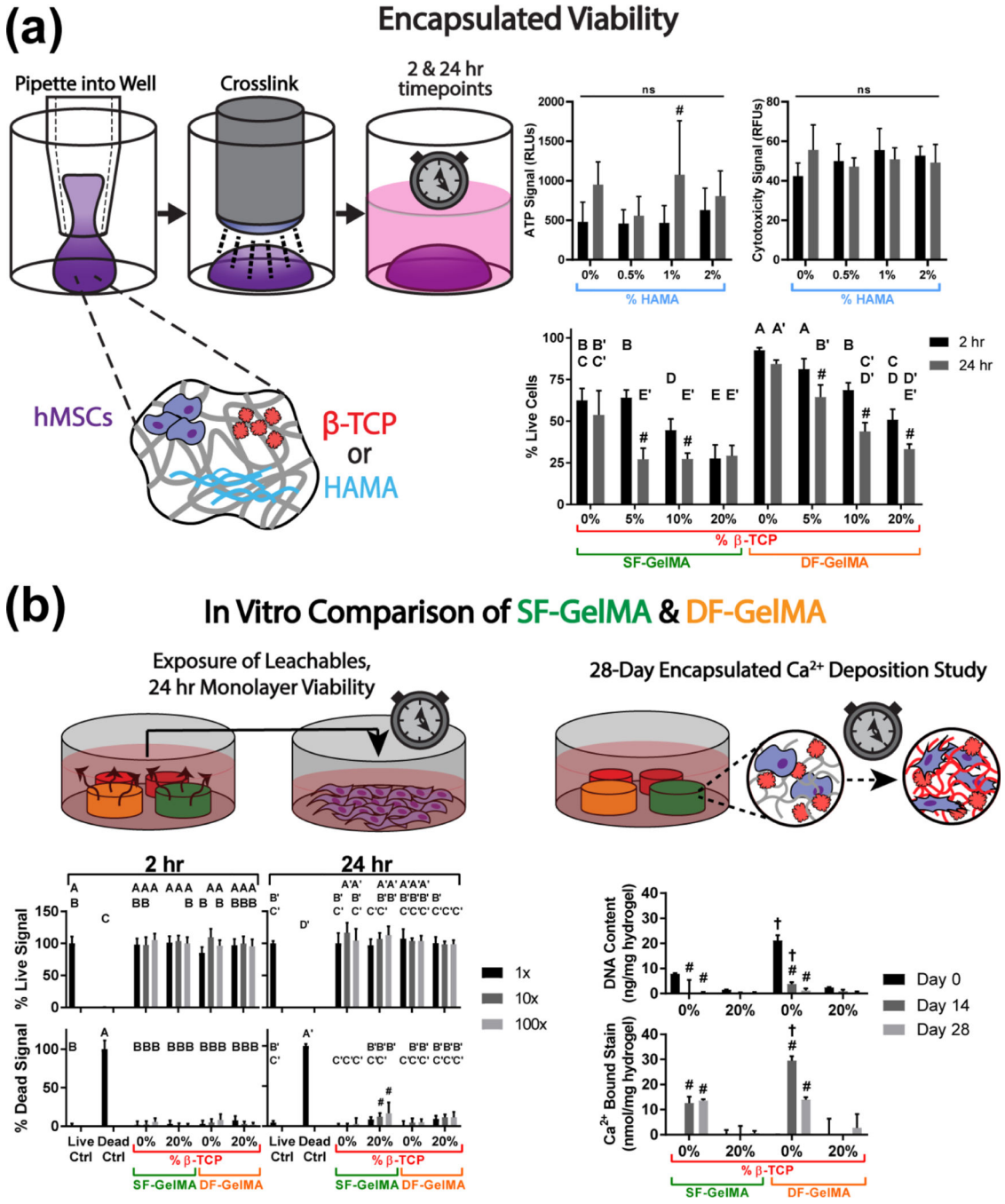

Figure 2.

(**a**) Scheme for examining viability of hMSCs within novel bioink formulations (left) next to the viability and proliferation data obtained via luminescent ATP assays, CellTox Green, and Live/Dead staining. Letters are the result of a post-hoc Tukey's HSD test; groups that do not share a letter are significantly different ($p<0.05$). Absence of tick marks indicates 2 hr comparisons, one tick mark indicates 24 hr comparisons. # indicates a significant difference compared to the 2 hr time point within the same groups. (**b**) Experiments focusing on the differences in biocompatibility outcomes based on gelMA backbone of the bioink. (**left**)

Quantified Live/Dead data from a study investigating the effect of leachable compounds obtained from crosslinked gelMA gels which include buffered β-TCP on the viability of hMSC monolayers. Letters are the result of a post-hoc Tukey's HSD test; groups that do not share a letter are significantly different ($p<0.05$). Absence of tick marks indicates 2 hr comparisons, one tick mark indicates 24 hr comparisons. # indicates a significant difference between 24 hr and 2 hr data within same group. (**right**) DNA content via PicoGreen and Ca^{2+} deposition data via Alizarin Red S staining from a 28-day hMSC-encapsulating osteogenic differentiation study with buffered β-TCP. # indicates a significant difference compared to day 0 within same group, and † indicates a significant difference between gelMA samples of the same β-TCP level within a timepoint ($p<0.05$).

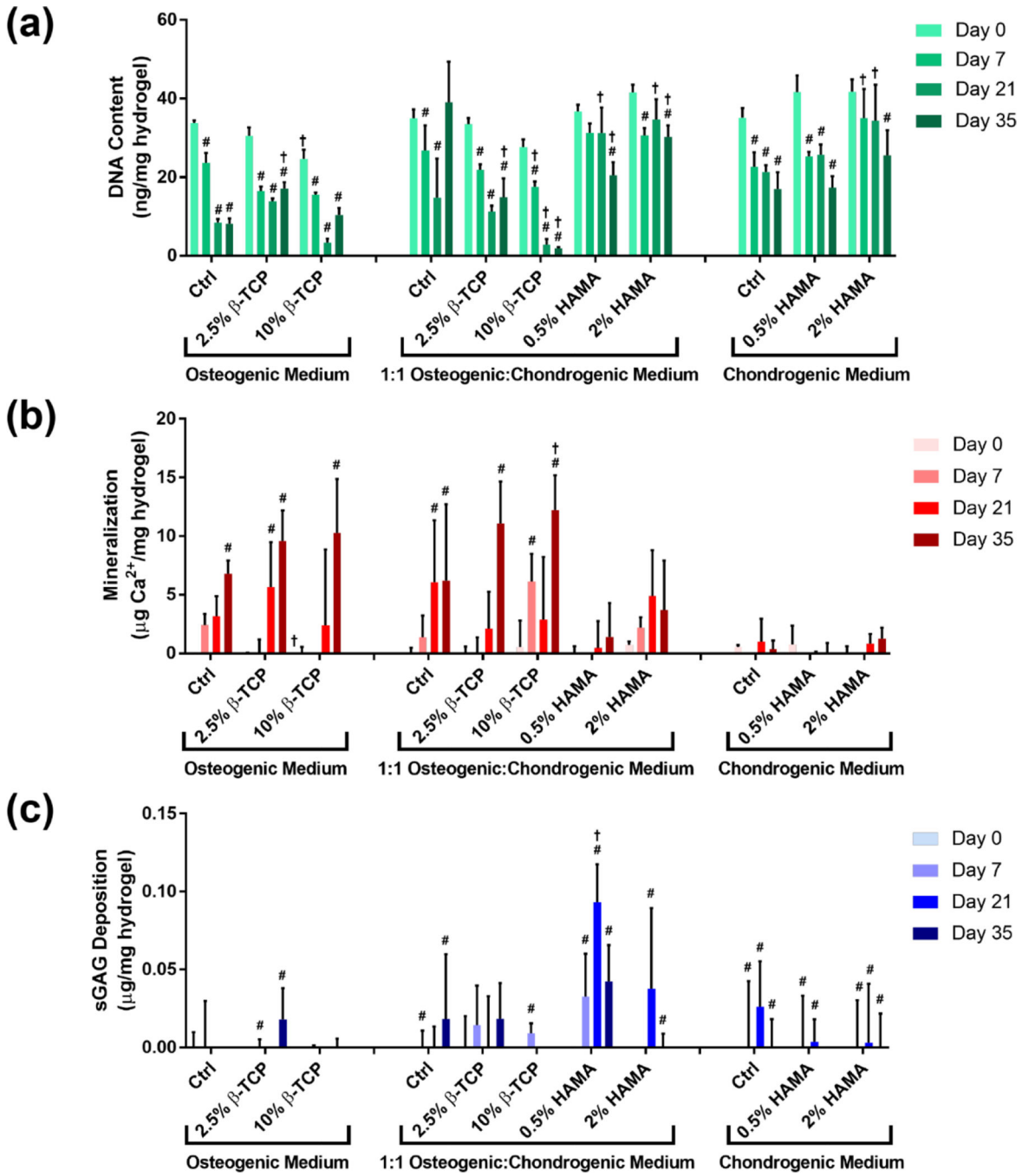

Figure 3.

DNA content and ECM deposition data from a 35-day differentiation study. (**a**) Data from a PicoGreen assay data showing the DNA content. (**b**) Arsenazo III assay data showing the Ca^{2+} content. (**c**) DMMB assay data showing the sGAG content (values below zero resulting from acellular sample subtraction are not shown). The readings from each sample were normalized to the wet weight of that hydrogel sample, and the values of the corresponding acellular controls have been subtracted. Significant differences are the result of separate two-way ANOVAs comparing either across timepoints within an experimental

group or comparing each experimental group to its control ($p < 0.05$). # indicates statistical significance between days 7 and 35 of the same group, and † indicates statistical significance relative to the culture medium's additive-free control group ($p<0.05$).

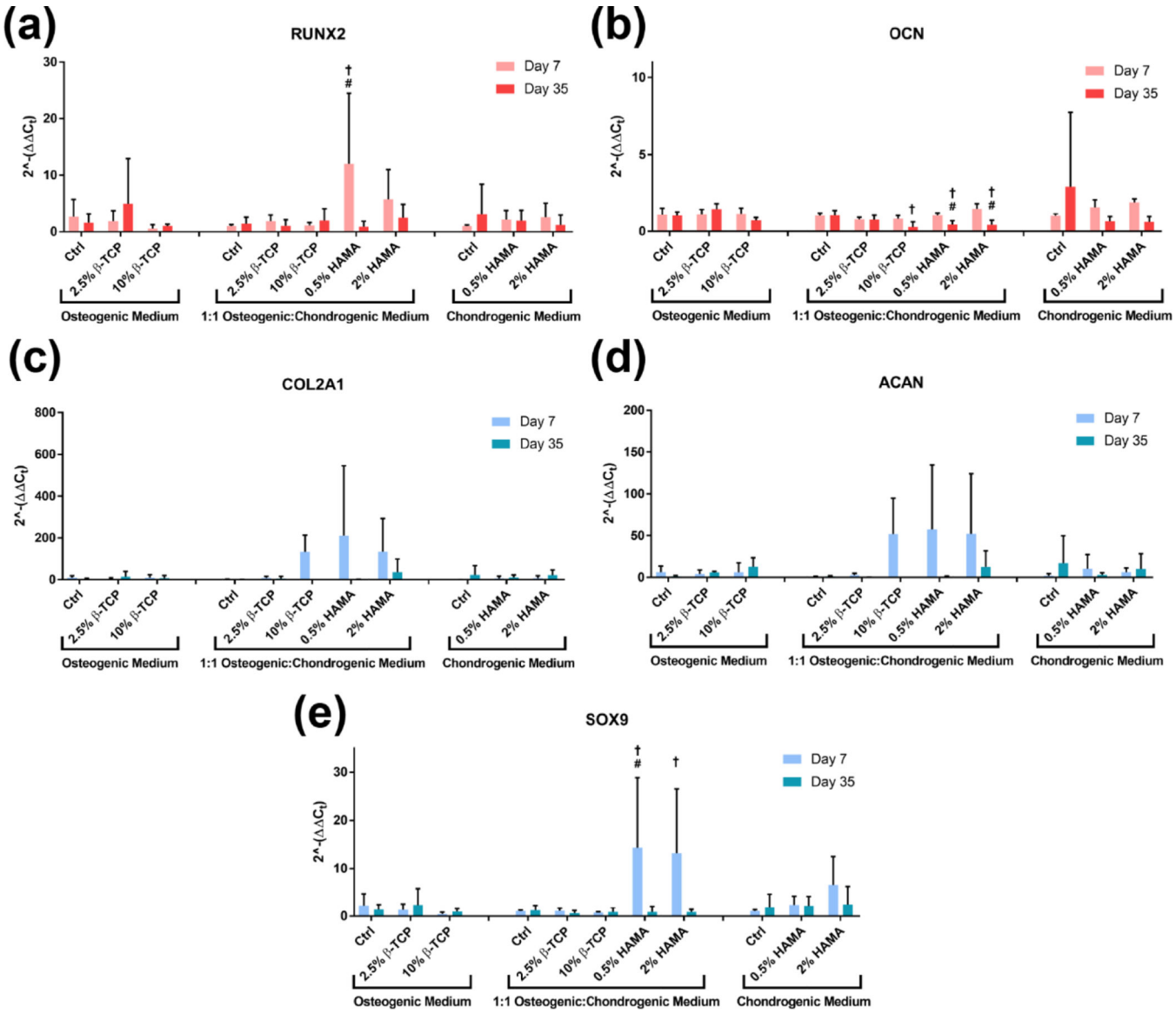

Figure 4.

After normalization to each sample's relative GAPDH expression, the data above summarizes the genetic expression via the Livak method of (**a**) the early/mid-stage osteogenic marker RUNX2; (**b**) the mid/late-stage osteogenic marker OCN; (**c**) the mid/late-stage chondrogenic marker COL2A1; (**d**) the mid/late-stage chondrogenic marker ACAN; (**e**) the early/mid-stage chondrogenic marker SOX9 of hMSCs encapsulated within novel bioink formulations, obtained via RT-qPCR. # indicates statistical significance between days 7 and 35 of the same group, and † indicates statistical significance relative to the culture medium's additive-free control group ($p<0.05$).

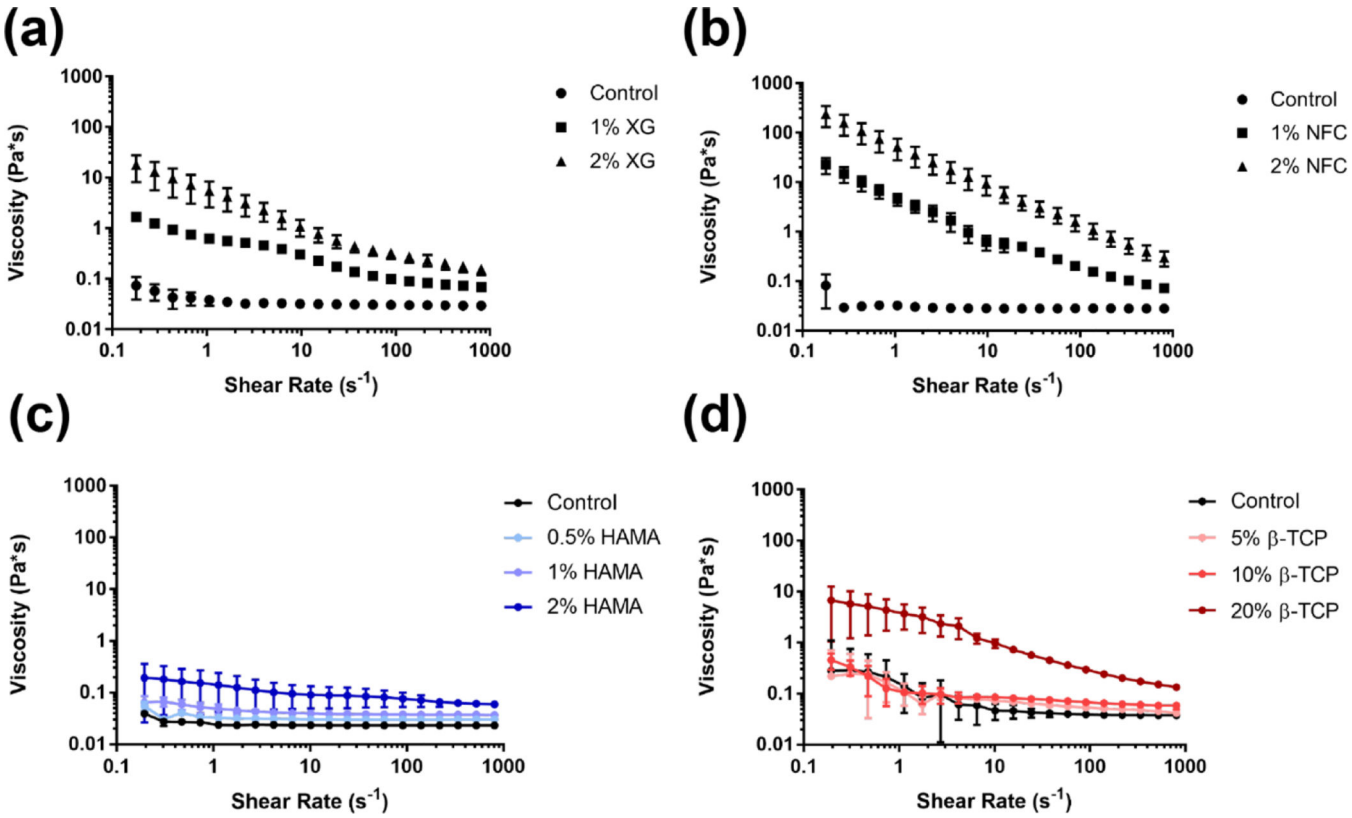

Figure 5.

Flow rheology data showing the effect of additives (**a**) XG, (**b**) NFC, (**c**) HAMA, and (**d**) β-TCP on novel bioink formulations' dynamic viscosity in response to increasing shear rate. Data is presented as the mean ± one standard deviation (n=3). All samples contained 10% w/v DF-gelMA.

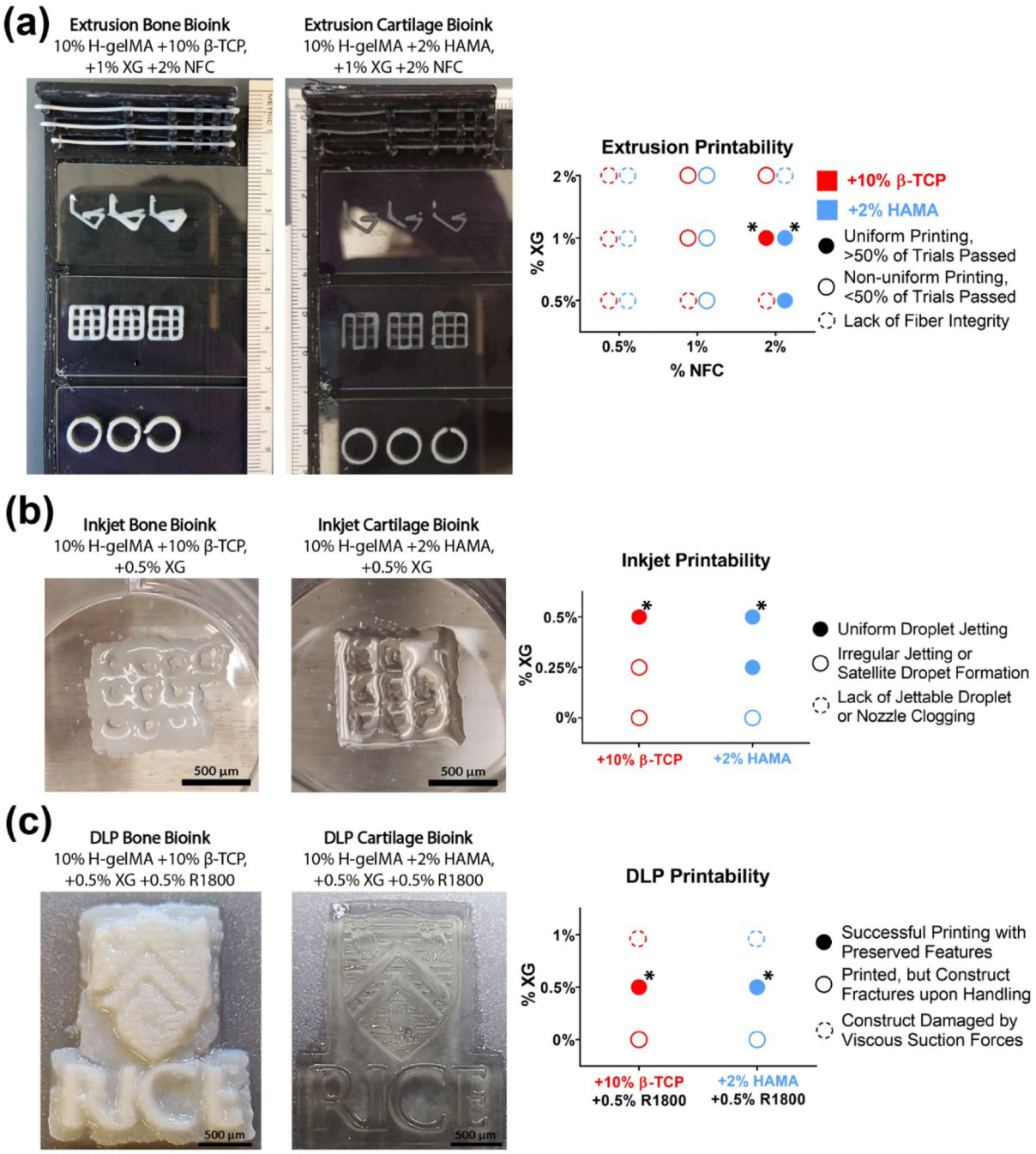

Figure 6.

Summary of printability results after inclusion of varying XG and NFC concentrations. From the qualitative printing trials, each row has the optimal tested β-TCP bioink trials (left), optimal tested HAMA bioink trial (middle), as well as an overall summary of printability trials (right) for (**a**) extrusion, (**b**) inkjet, and (**c**) DLP printing. * indicates the formulation chosen for cell-encapsulating bioprinting.

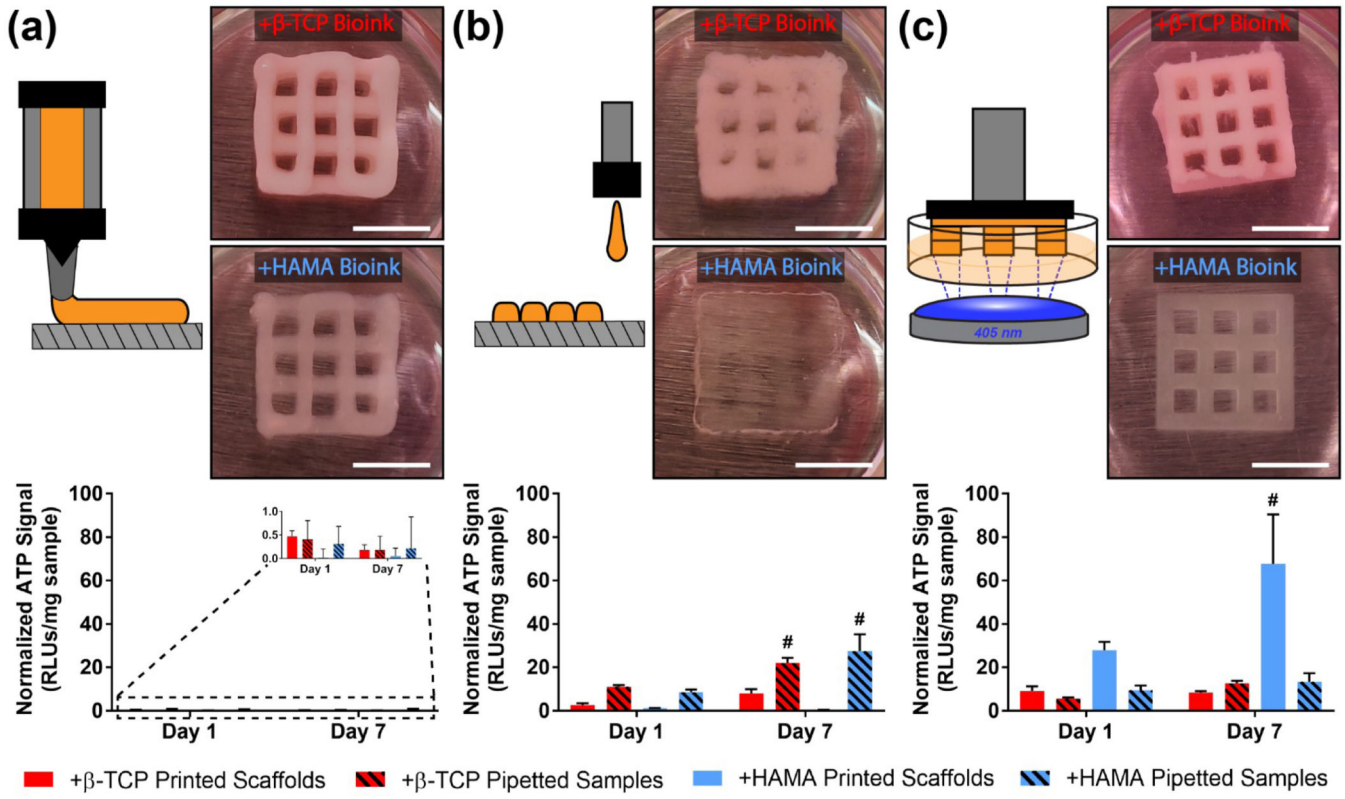

Figure 7.

Images of (**a**) extrusion, (**b**) inkjet, and (**c**) DLP bioprinted constructs after being cultured in media for seven days, shown above their normalized ATP content data from encapsulated hMSCs. Non-printed samples of the same bioink formulations were pipetted into well plates and crosslinked separately. # indicates a significant difference over time within the same experimental group ($p<0.05$). Scale bar = 5 mm.

Table 1:

Primer sequences for RT-PCR experiments.

Primer	Forward Sequence (5′ – 3′)	Reverse Sequence (5′ – 3′)	Amplicon Length
	Osteogenic Differentiation Markers		
RUNX2	TGGTTACTGTCATGGCGGGTA	TCTCAGATCGTTGAACCTTGCTA	101
OCN	TGCAGAGTCCAGCAAAGG	CCCAGCCATTGATACAGGTAG	93
	Chondrogenic Differentiation Markers		
ACAN	CCCCTGCTATTTCATCGACCC	GACACACGGCTCCACTTGAT	90
SOX9	AGCGAACGCACATCAAGAC	CTGTAGGCGATCTGTTGGGG	85
COL2A1	CAAACCCAAAGGACCCAAGTA	TGTGAGAGGGTGGGATGAA	100
	Housekeeping Genetic Marker		
GAPDH	CTGGGCTACACTGAGCACC	AAGTGGTCGTTGAGGGCAATG	101